Influence of structural Fe content in clay minerals on selenite redox reactions: Kinetics and structural transformations

Yanting Qian, Andreas C Scheinost, Sylvain Grangeon, Alwina Hoving, Sergey V Churakov, Maria Marques Fernandes

Geochimica et Cosmochimica Acta 377 (2024) 19–33

Contents lists available at ScienceDirect

Geochimica et Cosmochimica Acta

journal homepage: www.elsevier.com/locate/gca

Influence of structural Fe content in clay minerals on selenite redox reactions: Kinetics and structural transformations

Yanting Qian [a,b], Andreas C. Scheinost [c,d], Sylvain Grangeon [e], Alwina Hoving [f], Sergey V. Churakov [a,b], Maria Marques Fernandes [a,*]

[a] Laboratory for Waste Management, Paul Scherrer Institut, CH-5232 Villigen PSI, Switzerland
[b] Institute for Geological Sciences, University of Bern, CH-3012 Bern, Switzerland
[c] The Rossendorf Beamline at the European Synchrotron Radiation Facility (ESRF), Avenue des Martyrs 71, 38043 Grenoble, France
[d] Helmholtz Zentrum Dresden Rossendorf, Institute of Resource Ecology, Bautzner Landstrasse 400, 01328 Dresden, Germany
[e] BRGM – French Geological Survey, 45060 Orléans, France
[f] TNO Geological Survey of the Netherlands, PO Box 80015, 3508 TA Utrecht, The Netherlands

ARTICLE INFO

Associate editor: Mengqiang "Mike" Zhu

Keywords:
Selenite reduction
Fe(II)-bearing clay minerals
Red and grey elemental Se(0)
Kinetics
Redox potential

ABSTRACT

Redox reactions control the environmental fate of selenium, an element of concern due to its small gap between beneficial and detrimental effects on human health and due to the longevity of the radionuclide ^{79}Se produced in nuclear reactors. Fe-bearing clay minerals are major redox-active ingredients of Earth's critical zone and constitute an important component of the barrier in (radioactive and other) waste repositories. Here we systematically investigate selenite ($Se(IV)O_3^{2-}$) sorption and reduction by Fe-bearing clay minerals of the smectite group, using batch experiments and X-ray absorption fine structure (XAFS) spectroscopy to elucidate reaction mechanisms and kinetics up to 720 or 3600 h. We found a linear relationship between structural Fe(II) content and selenite reduction rate. Selenite reduction depends also on redox potential and pH, with pH 7 showing a slower reduction rate than at pH 5. Selenite first sorbs to clay edge sites by forming an inner-sphere sorption complex, before being reduced to Se(0). The first redox product was amorphous (red) Se(0), which gradually transformed into trigonal (grey) Se(0), indicative of a kinetically hindered conversion of an amorphous (or less crystalline) solid phase into the thermodynamically stable and more crystalline form of the solid. Despite an Fe_{aq}^{2+} concentration of up to $6{\cdot}10^{-4}$ M in the clay suspension, and their thermodynamic prediction for the clays at lower E_h, we did not observe formation of iron selenides. These insights into the selenite reduction mechanisms by Fe-bearing clays provides valuable information for the development of effective approaches for selenite immobilization.

1. Introduction

Selenium (Se) is a rare element in the earth's crust (0.05 mg/kg) and an important micronutrient for humans, having impact on cell function, antioxidant and immune systems (Titov et al., 2022). The gap between deficiency (< 40 μg/day) and toxicity (> 400 μg/day) of Se is very narrow (Winkel et al., 2012). Se deficiency can cause a series of health issues including hormonal imbalance in the thyroid, growth retardation, poor immune function, cancer, and increased mortality (Moreno-Reyes et al., 2001; Rayman, 2012). Endemic Se deficiency has been reported in China (Li et al., 2012) and Russia (Volfson et al., 2010). A daily dietary Se supplement of ~200 μg/day is recommended to prevent health issues (Hammouh et al., 2021). In contrast to Se deficiency, excess Se leads to Se poisoning symptoms such as garlic odor breath, discoloration of the skin, hair loss, fatigue, nausea, vomiting, and neurodegeneration (MacFarquhar et al., 2010).

Se is released into the ecosystem through both natural sources and anthropogenic activities. In terms of natural sources, Se is primarily found in sedimentary rocks and marine shale deposits, where it commonly exists as metal selenides and forms a minor part of metal-sulfur minerals. The weathering of these seleniferous rocks leads to Se oxidation and release into the environment (Fernández-Martínez and Charlet, 2009). Furthermore, volatilization by plants, bacteria and volcanic eruptions contribute to the natural release of Se in the gas phase.

* Corresponding author.
E-mail address: maria.marques@psi.ch (M. Marques Fernandes).

https://doi.org/10.1016/j.gca.2024.05.012
Received 7 December 2023; Accepted 13 May 2024
Available online 17 May 2024

As for anthropogenic sources, Se originates from activities such as coal and oil combustion facilities, selenium refining plants, base metal smelting and refining plants, mining and milling operations, as well as various end-product manufacturers (e.g., glass, semiconductors, and photovoltaic cells) (Fordyce, 2013; Tan et al., 2016). Besides the stable Se isotopes, radioactive ^{79}Se is a long-lived ($t_{1/2} = 3.27{\cdot}10^5$ years) fission product present in nuclear fuel (Bingham et al., 2011; Frechou et al., 2007). While Se occurs in the −II oxidation state in spent nuclear fuel (Curti et al., 2015), it is present in IV oxidation state in simulated vitrified waste (Curti et al., 2013).

Se deficiency and excess are highly influenced by the bioavailability of Se species in the environment, which in turn depends on the Se oxidation state. Se exists in five oxidation states: −II (selenide, Se^{2-}), −I (diselenide), 0 (elemental selenium), IV (selenite, SeO_3^{2-}), and VI (selenate, SeO_4^{2-}) (Ma et al., 2019). Selenate and selenite predominate at relatively high redox potential and are very soluble and mobile. Selenic (H_2SeO_4) and selenous (H_2SeO_3) acid are diprotic acids and the presence of their oxyanions $HSeO_4^-$, $HSeO_3^-$, SeO_3^{2-} depends on the solution pH. Elemental Se(0) is present at mild reducing redox potential as a stable non-soluble form, which can exhibit both amorphous and crystalline solids: red amorphous Se(0), and crystalline deep-red monoclinic and grey trigonal Se(0) (Fernández-Martínez and Charlet, 2009). Se(−I) and Se(−II) exist in reducing environment depending on pH as H_2Se, HSe^-, Se^{2-}, polyselenides Se_n^{2-}, and as poorly soluble metal selenides (Rojo et al., 2018; Scheinost and Charlet, 2008; Scheinost et al., 2008; Hummel and Thoenen, 2023). In contrast to the HSe^- anion (which is stable only in Fe-free systems), $FeSe_x$ species have a low solubility (log $K_{sp}(FeSe_2) = -13.4$, log $K_{sp}(FeSe) = -0.4$ (Hummel and Thoenen, 2023)), so in general, reduction is an efficient way to immobilize soluble Se.

Reduction of Se has been observed biotically and abiotically. Various bacteria carry out dissimilatory reduction to elemental Se(0) by using oxidized Se as electron acceptors to oxidize organic matter (Oremland and Stolz, 2000). Moreover, Se is also reduced abiotically by Fe minerals including magnetite (Jordan et al., 2009), mackinawite (Scheinost et al., 2008), and siderite (Scheinost and Charlet, 2008), green rust (Myneni et al., 1997), pyrite (Charlet et al., 2012; Curti et al., 2013; Rodriguez et al., 2020), troilite (Breynaert et al., 2008), Fe sorbed clay (Charlet et al., 2007), and zerovalent Fe(0) (Olegario et al., 2010). In the presence of above Fe(II)-bearing minerals, Se can be reduced to mostly red and grey elemental Se(0) and sometimes various iron selenides (FeSe) (Scheinost and Charlet, 2008) but rarely the most thermodynamically stable ferroselite ($FeSe_2$) (Charlet et al., 2012). The reduction is thought to proceed through a combined adsorption and redox process, since aqueous Fe^{2+} has little tendency to reduce selenite and selenate (Börsig et al., 2017; Charlet et al., 2012; Frasca et al., 2014). Selenite can be adsorbed through inner-sphere and outer-sphere complexation, depending on adsorbent and pH (Fernández-Martínez and Charlet, 2009; Jordan et al., 2014; Jordan et al., 2013). The reduction process and the final reduced Se species are governed by several factors such as pH, redox potential, kinetics, Se concentration, mineralogical composition of the environment, and biological interactions. Details about the reduction mechanism with respect to the electron transfer process and the control on the reduced species remain still vague, especially for the abiotic, mineral-surface-driven systems. Since batch sorption experiments are rarely sufficient to derive reduction mechanism, spectroscopic investigations such as X-ray absorption fine structure (XAFS) spectroscopy, including X-ray absorption near edge structure (XANES) and extended X-ray absorption fine structure (EXAFS), are now commonly used to elucidate both oxidation state and local structure of intermediate and final Se species. Furthermore, the reduction processes of selenite and to an even larger extent of selenate are slow and the reduced species may vary over time (Poulain et al., 2022). Therefore, long-term kinetic studies are needed to gain a better understanding of the reduction process from the early transient to long-term equilibrium states.

In this study, we investigate the role of structural Fe in clay minerals on the selenite reduction mechanism. Depending on its redox state, structural iron in clay minerals affects the physicochemical properties of clay minerals and is known to oxidize or reduce elements at their surface (by acting either as an electron donor or acceptor) thus altering their mobility and/or (bio)availability (Huang et al., 2021). We focus here on swelling clays of the smectite group, using reference samples provided by the Clay Source Repository of the Clay Minerals Society (Van Olphen et al., 1979), namely two natural montmorillonites (SWy-2 from Wyoming and STx-1 from Texas) because of their relevance for engineered barrier systems for radioactive waste repositories, and in addition a nontronite (NAu-2 from Australia), a natural Fe rich smectite, because of the abundant literature and datasets concerning its redox reactivity. We perform sorption experiments on these clay minerals reduced to different Fe(II)/Fe(III) ratios, to quantify the sorption and sorption kinetics of selenite on clay minerals. By applying XAFS, we would like to (1) follow the selenite reduction process, (2) identify the structure of sorbed species, and (3) elucidate the role of aqueous solution chemistry including pH and redox potential, to contribute to a wider understanding of Se immobilization in the environment.

2. Materials and methods

2.1. Clays

Three dioctahedral smectite clays with different Fe content, Texas montmorillonite STx-1, Wyoming montmorillonite SWy-2, and south Australian nontronite NAu-2, were purchased from the Clay Source Repository of the Clay Minerals Society (Purdue University, West Lafayette, IN). The chemical composition, structure, and Fe content of the raw material as provided by the Clay Mineral Society are listed in Table 1. The as-received clay materials were washed and purified to a homogeneous Na-form clay suspension in 0.1 M NaCl electrolyte. The detailed procedures are described in previous work (Qian et al., 2023).

2.2. Preparation of reduced clay suspensions

The three clay minerals were chemically reduced to obtain different Fe(II) contents associated with different redox potential (E_h) (Gorski et al., 2013). The reduction was conducted by the Citrate-Bicarbonate-Dithionite (CBD) method following Stucki et al. (Stucki et al., 1984) yet without heating. Purified clay suspensions were degassed with nitrogen gas (N_2) for two hours before transferring them into a N_2-atmosphere controlled anoxic glovebox ($O_2 < 0.1$ ppm). The complete reduction process was conducted in the glovebox. For STx-1, 500 mL clay suspension (22.18 g/L) were first mixed with a citrate-bicarbonate (CB) buffer solution (12 mL of 0.5 M $Na_3C_6H_5O_7{\cdot}2H_2O$ and 164 mL of 1 M $NaHCO_3$) in an infusion bottle for about an hour stirring. Afterwards, 2 g dithionite ($Na_2S_2O_4$) and 24 mL 0.1 M NaCl were added to a total volume of 700 mL. For SWy-2, the same procedures were carried out with 1 L clay suspension (14.32 g/L), 500 mL of 1 M $Na_3C_6H_5O_7{\cdot}2H_2O$, 250 mL of 1 M $NaHCO_3$, and 34.52 g $Na_2S_2O_4$ with a total volume of 1700 mL. The clay suspensions were stirred for about one day after adding dithionite. After reduction, clay suspensions were washed in

Table 1
Chemical composition and structure of STx-1, SWy-2, and NAu-2 provided by the Clay Minerals Society (Van Olphen et al., 1979).

Clay	Chemical formula. The first round bracket denominates the charge-compensating interlayer cations, the first square bracket the octahedrally coordinated cations, and the second square bracket the tetrahedrally coordinated cations of the TOT layers
STx-1	$(Ca_{0.27}Na_{0.04}K_{0.01})[Al_{2.41}Fe(III)_{0.09}Mn_{tr}Mg_{0.71}Ti_{0.03}][Si_{8.00}]O_{20}(OH)_4$
SWy-2	$(Ca_{0.12}Na_{0.32}K_{0.5})[Al_{3.01}Fe(III)_{0.41}Mn_{0.01}Mg_{0.54}Ti_{0.02}][Si_{7.98}Al_{0.02}]O_{20}(OH)_4$
NAu-2	$(M^{\square}_{0.97})[Al_{0.52}Fe_{3.32}\ Mg_{0.7}][Si_{7.57}Al_{0.01}Fe_{0.42}]\ O_{20}(OH)_4$

dialysis bags first with 1 M NaCl at pH 4 to remove added chemicals and dissolved elements, and then with 0.1 M NaCl without pH adjustment until the concentration of citrate and bicarbonate were less than 10^{-9} M, which is the calculated concentration based on dilution through the 25 washing steps. For NAu-2, two reduction degrees (low-reduced NAu-2 and high-reduced NAu-2) were prepared, and the details are described in previous work (Qian et al., 2023). Overall, an S/Fe molar ratio of 10 was used for reduced STx-1, reduced SWy-2, and high-reduced NAu-2, while an S/Fe molar ratio of 0.5 was used for low-reduced NAu-2. Finally, the suspension of reduced clays in 0.1 M NaCl matrix were stored in the glovebox in infusion bottles covered with aluminum foil to avoid photo oxidation. The chemical composition in weight percentage (wt%) of the as prepared native and reduced samples were determined using X-Ray Fluorescence (XRF) spectroscopy. The Fe(II) wt% content was calculated based on the reduction level of each clay and is presented in Table 2.

2.3. Cation exchange capacity and edge site availability

To ensure that the CBD treatment did not alter the sorption properties of the three clays, their cation exchange capacity (CEC) and their surface complexation ability were quantified. The CEC of native and reduced clays were directly quantified using the highly selective divalent nickeltriethylenediamine (Ni-en) complex radiolabelled with ^{63}Ni (Peigneur, 1976). At sufficiently high concentration, this index cation is expected to completely displace and replace all the cations present on the exchange sites of clay minerals. The whole experiment was carried out in the glovebox ($O_2 < 0.1$ ppm) and all the solutions were degassed with N_2 before transferring into the glovebox. A Ni-en solution was prepared as a mixture of nickel nitrate $Ni(NO_3)_2$ and ethylene diamine $C_2H_4(NH_2)_2$ labelled with ^{63}Ni. The clay suspension (~6 g/L) was mixed with ^{63}Ni-en solution (200 mL 0.02 M Ni-en solution at pH 8 and 50 µL $4.5{\cdot}10^{-5}$ M ^{63}Ni tracer solution) in a centrifuge tube (Backman 26 mL) to a total volume of 22 mL. After 4 h continuously end-to-end shaking, the samples were centrifuged at 40,000 g (Backman Coulter Optima™ L-100 XP Ultracentrifuge, 70 Ti rotor) for one hour. The activity in the supernatant was measured using a beta liquid scintillation counter (Tri-Carb 4910 TR), and the pH was determined using a Metrohm electrode (model: 6.0232.100). The Ni-en adsorbed (Ni-en_{ads}) in meq/kg (equal to the CEC) is calculated from the redistribution of the radiotracer between the solid and liquid phases and is calculated from equation (1):

$$\text{Ni}-\text{en}_{ads} = \frac{A_{in} - A_{out}}{A_{in}} \cdot \text{Ni}-\text{en}_{in} \quad (1)$$

where A_{in} = initial ^{63}Ni activity (cpm), A_{out} = final ^{63}Ni activity (cpm), and Ni-en_{in} = initial amount of Ni-en (meq/kg).

The availability of the edge sites of native and reduced clays for cation surface complexation was assessed by measuring the sorption of Eu(III) (Baeyens and Bradbury, 2004). This trivalent cation was chosen to avoid competitive sorption effects with Fe(II) (Marques Fernandes and Baeyens, 2020; Soltermann et al., 2014). Note that although the reducing agents were washed away after reduction, Fe^{2+} unavoidably dissolved from the clay itself and established equilibrium with the clay suspension, potentially re-adsorbing onto the clay surfaces depending on pH, which would result in a reduced sorption capacity for other divalent cations, while trivalent cations like Eu(III) are less affected. The sorption of Eu(III) on the samples was quantified by radiochemical assay using ^{152}Eu. Eu sorption isotherms were measured at a series of Eu concentrations using both active ^{152}Eu and stable Eu ($Eu(NO_3)_3{\cdot}5H_2O$) between $1{\cdot}10^{-7}$ M and $2{\cdot}10^{-4}$ M at 2 g/L and pH ~ 7 in 0.1 M NaCl and equilibrated for 7 days. Due to the high buffering capacity of reduced clays, the pH of the suspensions was adjusted with HCl and NaOH before sorption experiments. Afterwards, Eu solution, clay suspension, pH buffer ($2{\cdot}10^{-3}$ M MOPS (3-(Nmorpholino) propanesulfonic acid), and 0.1 M NaCl were combined in centrifuge tubes to a total volume of 22 mL and sealed. After 7 days end-to-end continuous shaking, tubes were centrifuged at 40,000 g for one hour to separate the clay and the supernatant. Two aliquots of the supernatant were taken immediately for radiochemical assays of ^{125}Eu using a gamma counter (WIZARD^2, 2480). The pH of the supernatant was measured with Metrohm electrodes. Each experiment was carried out in duplicate. The sorbed amount of Eu is calculated by equation (2).

$$\text{Sorbed} = [C_{init}] - [C_{eql}] \cdot \frac{V}{m} \quad (2)$$

Where C_{init}: initial concentration of active and inactive Eu (M), C_{eql}: equilibrium concentration of active and inactive Eu (M), V: total volume of the liquid phase (L), m: mass of the solid (kg).

2.4. Se sorption and reduction kinetics

To quantify the uptake of Se, batch type sorption and reduction kinetic experiments were carried out without replicates in a N_2 atmosphere controlled anoxic glovebox ($O_2 < 0.1$ ppm) at room temperature and over different time periods from 4 h to 3600 h. Reduced SWy-2 and high-reduced NAu-2 are up to 3600 h, while reduced STx-1 and low-reduced NAu-2 are up to 720 h. A solid to liquid ratio of 2 g/L was used in all the experiments, allowing XAS measurements and sorption quantification under the same conditions.

Sorption and reduction kinetics were conducted with a Na_2SeO_3 concentration of $3{\cdot}10^{-5}$ M at pH 5 in 0.1 M NaCl. This Se concentration was chosen to obtain sorption loadings sufficiently high to be measured by XAFS spectroscopy. The pH of the clay suspensions was adjusted accordingly before sampling experiment. Acetate pH buffer ($2{\cdot}10^{-3}$ M $CH_3COONa{\cdot}3H_2O$), 0.1 M NaCl, and Na_2SeO_3 solution were added to a 250-mL infusion bottle. Acetate buffer is chosen because of its weak tendency to complex with metal ions (Perrin and Dempsey, 1974). Bradbury and Baeyens (2002) have tested that there was no significant influence of $2{\cdot}10^{-3}$ M acetate buffer on sorption. Slow end-to-end shaking was employed. At the end of the different equilibration times, samples were transferred into centrifuge tubes and centrifuged at 40,000 g for one hour to separate the clay from the supernatant. A portion of the supernatant was sampled for Se concentration analysis using ICP-OES and for Fe^{2+} concentration ($[Fe^{2+}_{eql}]$) analysis with phenanthroline ($C_{12}H_9ClN_2{\cdot}H_2O$) through UV–VIS spectrophotometry. The remaining supernatant was used to measure pH. The clay sediments (wet pastes) were filled in High Density Polyethylene (HDPE) XAFS sample holders and covered with Kapton tape. The sorption of Se is expressed by the logarithm of the solid–liquid distribution coefficient R_d (L/kg) defined in equation (3).

$$Rd = \frac{[C_{init}] - [C_{eql}]}{[C_{eql}]} \cdot \frac{V}{m} \quad (3)$$

Where C_{init}: initial concentration of Se (M), C_{eql}: equilibrium concentration of Se (M), V: total volume of the liquid phase (L), m: mass of the solid phase (kg).

The uncertainty on distribution coefficient R_d was calculated with an error propagation method following Tournassat et al. (2013).

2.5. X-ray absorption spectroscopy

Clay pastes for XAFS were transferred into a liquid N_2 Dewar for flash freezing right after preparation in the glovebox, where they remained for storage and transport to the beamline to conserve the chemical equilibrium at the sampling state and anoxic conditions. At the beamline, they were quickly transferred to a closed-cycle He cryostat used for the XAFS measurements, always maintaining a frozen state.

The XAFS measurements were conducted at the Rossendorf Beamline (ROBL) BM20 of the European Synchrotron Radiation Facility (ESRF), France (Scheinost et al., 2021). The X-ray beam was monochromatized

by a Si(1 1 1) double–crystal monochromator, and the energy of monochromator was calibrated with an Au foil using the Au L_3-edge at 11,919 eV. 8 samples were loaded at the same time on an automated sample holder and inserted into the closed-cycle He-cryostat (CryoVac). Se-K edge XANES and EXAFS spectra were collected in fluorescence mode at 15 K with an 18-element Ge-detector (Mirion) and a Falcon-X (XIA) electronic spectrometer. Each sample was scanned repeatedly for several times to obtain sufficient statistics. The XAS spectra were collected in step-scan mode with a counting time of 1 s per step across pre-edge and XANES regions, and then increasing from 2 to 14 s per step across the EXAFS (k) region as a square function of the photon wavevector, with a total collection time of 42 min per scan. Depending of Se concentration, between 2 and 8 scans were collected to obtain acceptable noise levels especially at high k-range. Energy correction and averaging of individual scans were performed in Sixpack (Webb, 2005). Fluorescence dead time correction was applied to all the sample spectra measured in fluorescence mode. The averaged spectra were then processed in WinXAS (Ressler, 1998) using standard procedures. The spectra were normalized by 1st and 2nd order polynomial fits before and after the absorption edge, respectively. The energy threshold E_0 was determined by the first inflection point of the absorption edge for conversion into k space, and the EXAFS spectrum was then extracted by using a cubic-spline fit from 2 to 13 $Å^{-1}$ at k^3 weight, using the AutoSpline functionality of WinXAS. Statistical analyses (principal component analysis, VARIMAX rotation, iterative target test transformations) were performed with the ITFA software package (Rossberg et al., 2003) for quantitative speciation using both XANES and k^3-weighted EXAFS spectra (note that only the latter data are reported, but both methods yielded similar results within the error of 5%). EXAFS shell fitting was conducted in WinXAS in R space (k^3 weight, Bessel window, k range 2–12 $Å^{-1}$).

2.6. Mediated electrochemical reduction and oxidation

Mediated electrochemical reduction (MER) and oxidation (MEO) were performed at TNO, Utrecht, to measure redox-active Fe in the clay mineral samples and to derive their apparent E_h using the method described by Gorski et al. (Gorski et al., 2012; Gorski et al., 2013). A three-electrode setup was used having a glassy carbon crucible working electrode, a 3 M NaCl Ag/AgCl reference electrode and a platinum counter electrode separated from the working electrode compartment by a porous glass frit (Hoving et al., 2017). All experiments were carried out in a pH 7 buffered solution (0.1 M NaCl, 0.01 M MOPS buffer, pKa = 7.2). The stability of the mediators at pH 5 could not be guaranteed, as there was a color change in the buffer solution after measurements. Consequently, the E_h of the clays was not measured at pH 5. A constant potential was applied on the electrochemical cell. Subsequently, an electron transfer mediator was added to facilitate electron transfer between the working electrode and Fe in the clay mineral. After equilibration of the mediator with the applied potential, the clay mineral suspension was added to the cell. The extent of structural Fe reduction or oxidation was determined by integrating the current peak response (electron accepting capacity (EAC) and electron donating capacity (EDC)). Redox profiles were constructed by measuring the EAC and EDC at a wide range of different applied potentials. To ensure proper electron transfer, mediators were used at applied potentials within ±0.12 V of their E_h^0-values (Gorski et al., 2013). The following mediators were used: ABTS (2,2′-azino-bis(3-ethylbenzothiazoline-6-sulphonic acid), ferri/ferro-cyanide ($Fe^{2+/3+}(CN)_6$), DCPIP (2,6-dichlorophenolindophenol), hexaammineruthenium ($Ru^{2+/3+}(NH_3)_6$), resorufin, riboflavin 5′-monophosphate, zwitterionic viologen (4,4′-bipyridinium-1,1′-bis(2-ethylsulfonate)), and triquat (1,1′-trimethylene-2,2′-bipyridyl). The resulting redox profiles of the various clay mineral samples were fitted using a modified form of the Nernst equation (Eq. (2) in Gorski et al., 2013). From these fitted curves the apparent reduction potential was derived.

3. Results and discussion

3.1. Clay characterization

In a previous study, we compared the morphology of the native and CBD-reduced Fe-bearing phyllosilicates and observed no significant change. Only a limited dissolution of the external layers from the clay platelets could be identified (Qian et al., 2023). To assess the potential impact of this slight external surface dissolution on the chemical properties of the different clays, we measured the CEC with Ni-en and Eu(III) sorption isotherms to compare the surface complexation on edge sites between the native and the reduced clays. The high selectivity of the Ni-en complex for the cation exchange sites, allows us to assess the CECs of the native and reduced clays (Table 2). No significant difference of CEC between native and reduced clays were observed, indicating that the cation exchange sites of reduced clays were not significantly affected by the reduction process.

Fig. 1 shows the sorption isotherms of Eu(III) in the pH range 7.0–7.3 for the different native and reduced clays. The Eu sorption was predicted using the 2 site protolysis non-electrostatic surface complexation and cation exchange (2SPNE SC/CE) model for montmorillonite (Baeyens and Marques Fernandes, 2018) and is shown as black line in Fig. 1. Note the nonlinear shape indicating adsorption to both strong and weak sorption sites. Our sorption data for the different native and reduced clays agree well with this previously determined model for montmorillonite. Except for a slightly higher Eu sorption (~0.5 log units) on high-reduced NAu-2, no significant variation in Eu sorption between native and reduced clays could be identified. The slightly higher Eu sorption on high-reduced NAu-2 is likely due to the higher pH of this isotherm (7.3 compared to 7.0–7.1), since in 0.1 M NaCl the sorption of positively charged cations adsorbing via surface complexation raises sharply in the pH range 6–8 (Baeyens and Marques Fernandes, 2018; Jaisi et al., 2008), hence our conclusion is that Fe reduction by the CBD method did not affect sorption to the edge sites of the clay.

Table 2
Clay characterization (Redox active and inactive Fe as measured by MEO/MER, CEC as determined by the Ni-en method).

Clay	$Fe(II)/Fe_{tot}$	$Fe(III)/Fe_{tot}$	Redox inactive Fe/Fe_{tot}	Fe(II) wt%	Fe(II) $mmol/kg_{clay}$	CEC meq/kg
High-reduced NAu-2	0.58 ± 0.03	0.12 ± 0.01	0.30 ± 0.02	11.4 ± 0.4	2040 ± 73	1125 ± 23
Low-reduced NAu-2	0.19 ± 0.01	0.45 ± 0.01	0.34 ± 0.01	4.2 ± 0.1	740 ± 7	1137 ± 10
Native NAu-2	0.00 ± 0.00	0.75 ± 0.02	0.25 ± 0.01	0.0 ± 0.0	0 ± 0	1050 ± 67
Reduced SWy-2	1.00 ± 0.04	0.00 ± 0.00	0.00 ± 0.00	2.5 ± 0.1	450 ± 16	1247 ± 19
Native SWy-2	–*	–	–	0.0*	0	1239 ± 46
Reduced STx-1	0.89 ± 0.01	0.00 ± 0.00	0.11 ± 0.01	0.6 ± 0.1	100 ± 9	1202 ± 12
Native STx-1	–*	–	–	0.0*	0	1247 ± 58

* The native SWy-2 and STx-1 were not measured by MEO/MER. All the existing Fe in the native SWy-2 and STx-1 is in Fe(III) state given by the Clay Minerals Society in Table 1.

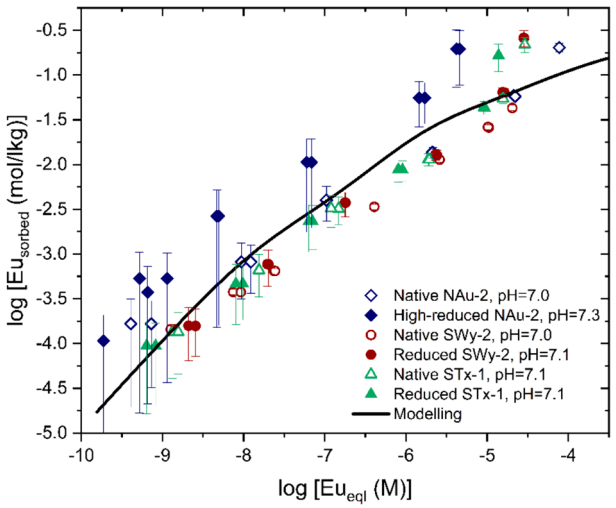

Fig. 1. Eu(III) sorption isotherm on native and reduced NAu-2, SWy-2, and STx-1 in 0.1 M NaCl, S/L of 2 g/L, and ~pH 7. The modelling curve is based on parameters taken from (Baeyens and Marques Fernandes, 2018).

3.2. Sorption and reduction kinetics

Preliminary sorption studies (Fig. S1) showed that after 7 days, selenite uptake by reduced clays was comparable to that obtained for non-reduced clays (Missana et al., 2009). The sorption of selenite after 7 days (Fig. S1a) decreases as the pH increases from 4 to 8. Missana et al. modelled the data with a simple one-site model (complexes with only weak sites), assuming surface complexation pH < 8 (Missana et al., 2009). Due to the repulsion of the selenite anion on the deprotonated clay surface, the sorption drops dramatically at pH > 8. Previous studies have shown, however, that the Se reduction is kinetically controlled (Charlet et al., 2007; Onoguchi et al., 2019; Pearce et al., 2008). Therefore, we investigated sorption and reduction kinetics on reduced clays up to several months. For these kinetics experiments, we chose a pH of 5 (Fig. S1a) and an initial Se concentration of $3{\cdot}10^{-5}$ M to obtain sufficient Se loadings (Fig. S1b) to be able to study their speciation with XAFS.

Fig. 2 shows the sorption and reduction kinetics of reduced clays from 4 h to 3600 h. The sorption results are listed in Table 3. The

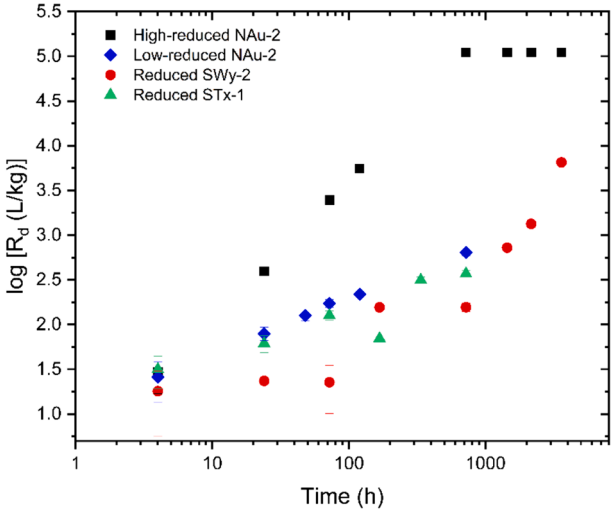

Fig. 2. Selenite uptake kinetics on reduced clay samples at S/L of 2 g/L, $[Se]_{init} = 3{\cdot}10^{-5}$ M, pH = 5, 2 mM acetate buffer, and 0.1 M NaCl. If error bars are not visible, they are smaller than symbol sizes. Selenite sorption in ppm is shown in Fig. S2.

sorption of selenite on reduced clays increases with contact time, indicating a kinetically controlled uptake reaction, consistent with previous observations (Charlet et al., 2007; López de Arroyabe Loyo et al., 2008; Myneni et al., 1997). High-reduced NAu-2 which has with 11.4 wt% the highest amount of Fe(II), shows also a significantly higher selenite uptake than the other reduced clays, achieving complete uptake of selenite achieved after 720 h. Reduced SWy-2 exhibited lower sorption, which gradually increased over a period of 3600 h without reaching a plateau. Low-reduced NAu-2 and reduced STx-1 seem to show a similar behavior, although values of 1440 h, 2160 h, and 3600 h are not available due to contamination. Clearly, selenite sorption on reduced clays requires considerably long equilibration time, suggesting that Se(IV) might be gradually reduced after adsorption on the Fe(II)-bearing clays (Charlet et al., 2007). To further explore the evolution of selenite uptake, presumably by reduction, we followed the sorption kinetics with XAFS.

3.3. Se K-edge XAFS measurements of kinetic clay samples

To follow the kinetics of Se oxidation state, we performed Se K-edge XANES spectroscopy. The temporal evolution of the four reduced clay samples is shown in Figs. 3–6 (a) along with selenite (Se(IV)), red Se(0) and grey Se(0) reference spectra. The Se(IV) reference is selenite sorbed to each respective native clay at pH 5, while red Se(0) and grey Se(0) reference are retrieved from previous publications (Charlet et al., 2007; Scheinost and Charlet, 2008; Scheinost et al., 2008). The XANES spectra of sorbed Se(IV) on each type of clay vary from that of Se(IV) in solution (Fig. S3) in the region 12.66–12.69 keV. Moreover, Peak et al. (2006) showed significant variations in the XANES spectra of aqueous SeO_3^{2-}, $HSeO_3^-$, H_2SeO_3. Therefore, we used the spectrum of sorbed Se(IV) collected under the same experimental conditions as reference for the subsequent statistical analyses to exclude the influence of Se(IV) speciation and molecular geometry changes due to sorption. By looking at the two white line positions for Se(IV) and Se(0) (marked by hatched lines), the XANES spectra allow to directly follow the evolution of the oxidation state of selenium across time. Except for high-reduced NAu-2, which is already largely reduced at this stage, the samples of the shortest reaction time (4h) show the Se(IV) white line, which then gradually transform into Se(0) white lines.

While XANES alone would be sufficient to discriminate between Se at oxidation states 0 and IV, further details about the exact chemical structure of sorption complexes can be derived by analyzing the EXAFS spectra (see k^3-weighted EXAFS chi function in subfigures (b) of 3–6, and their corresponding Fourier Transform Magnitudes (FTM) in subfigures (c) of Figs. 3–6). The chi spectra of selenite are dominated by oscillations in the low k-range arising from backscattering of the Se-O pairs of the selenite molecule, whereas Se(0) spectra are dominated by oscillations in the high k-range arising from backscattering of the (nearest neighbor) Se-Se pairs of elemental selenium.

In the FTM spectra, the peak at approximately 1.3 Å (distance not corrected for phase shift) represents the Se(IV)-O interaction. Red and grey Se(0) can easily be distinguished since red Se(0) exhibits only one peak at around 2.0 Å (uncorrected for phase shift) representing the nearest Se-Se pairs, while grey Se(0) displays an additional peak at approximately 3.1 Å (uncorrected for phase shift) arising from next nearest Se-Se pairs and hence representing the longer range order of crystalline, grey elemental Se. In fact, all three FTM peaks occur in our set of clay samples with temporal evolution, indicating the presence of selenite and of red and grey elemental selenium.

To further elucidate the presence of different chemical species and to retrieve their statistical distribution among the different clay samples, we performed an in-depth analysis using ITFA (Rossberg et al., 2003). The number and identity of representative species in each kinetic clay series was based on principal component analysis, the Malinoswki indicator, and the visual inspection of the reconstruction (red lines) of the experimental spectra (black lines) with a minimum of components (Figs. 3–6). More details of the procedure can be found e.g. in Yalçıntaş

Table 3
Kinetics of selenite sorption and reduction; fraction of reduction products resulted from ITT.

pH	Time	[a][Se]$_{eql}$	[b]log Rd	Se loading	[c]Se(IV)	[c]Red Se(0)	[c]Grey Se(0)
	Hour	M	L/kg$_{clay}$	mmol/kg$_{clay}$	Fraction	Fraction	Fraction
Reduced STx-1 (Fe(II)$_{str}$: 100 mmol/kg, [Fe^{2+}_{eql}] ≈ 2·10^{-5} M, k* = 0.00215 h^{-1} at pH 5)							
5	4	2.35·10^{-5}	1.50	0.74 ± 0.06	1.00	0.00	0.00
5	24	2.22·10^{-5}	1.79	1.37 ± 0.12	0.76	0.24	0.00
5	72	1.99·10^{-5}	2.10	2.52 ± 0.22	0.42	0.58	0.00
5	168	2.12·10^{-5}	1.85	1.49 ± 0.13	0.32	0.68	0.00
5	336	1.53·10^{-5}	2.50	4.82 ± 0.42	0.26	0.74	0.00
5	720	1.43·10^{-5}	2.57	5.31 ± 0.46	–[‡]	–	–
		[Fe^{2+}_{eql}] ≈ 10^{-6} M at pH 7					
7	168	2.13·10^{-5}	1.94	1.84 ± 0.16	0.79	0.21	0.00
7	1440	1.12·10^{-5}	2.79	6.84 ± 0.60	0.11	0.77	0.12
Reduced SWy-2 (Fe(II)$_{str}$: 450 mmol/kg, [Fe^{2+}_{eql}] ≈ 10^{-5} M, k* = 0.00576 h^{-1} at pH 5)							
5	4	2.41·10^{-5}	1.26	0.44 ± 0.04	–[‡]	–	–
5	24	2.39·10^{-5}	1.37	0.56 ± 0.05	0.79	0.20	0.01
5	72	2.39·10^{-5}	1.35	0.54 ± 0.05	0.66	0.34	0.00
5	168	1.79·10^{-5}	2.19	2.97 ± 0.26	0.00	0.94	0.06
5	720	1.90·10^{-5}	2.19	2.97 ± 0.26	0.16	0.75	0.09
5	1440	1.01·10^{-5}	2.86	7.34 ± 0.64	0.10	0.83	0.07
5	2160	6.74·10^{-6}	3.13	9.02 ± 0.78	0.09	0.82	0.09
5	3600	1.76·10^{-6}	3.81	11.47 ± 1.00	0.00	0.01	0.99
		[Fe^{2+}_{eql}] ≈ 3·10^{-6} M at pH 7					
7	168	2.17·10^{-5}	1.78	1.29 ± 0.11	0.58	0.36	0.06
7	1440	1.33·10^{-5}	2.64	5.77 ± 0.50	0.05	0.26	0.68
Low-reduced NAu-2 (Fe(II)$_{str}$: 740 mmol/kg, [Fe^{2+}_{eql}] ≈ 5·10^{-5} M, k* = 0.04306 h^{-1} at pH 5)							
5	4	2.37·10^{-5}	1.42	0.62 ± 0.05	1.00	0.00	0.00
5	24	2.15·10^{-5}	1.90	1.71 ± 0.15	0.03	0.97	0.00
5	48	1.99·10^{-5}	2.10	2.51 ± 0.22	0.03	0.97	0.00
5	72	1.85·10^{-5}	2.24	3.19 ± 0.28	0.04	0.96	0.00
5	120	1.73·10^{-5}	2.34	3.79 ± 0.33	0.06	0.94	0.00
5	720	1.09·10^{-5}	2.81	6.95 ± 0.60	0.00	1.00	0.00
High-reduced NAu-2 (Fe(II)$_{str}$: 2040 mmol/kg, [Fe^{2+}_{eql}] ≈ 6·10^{-4} M, k* = 0.22679 h^{-1} at pH 5)							
5	4	2.36·10^{-5}	1.47	0.70 ± 0.06	0.09	0.84	0.07
5	24	1.40·10^{-5}	2.60	5.53 ± 0.48	–[‡]	–	–
5	72	4.21·10^{-6}	3.39	10.41 ± 0.91	0.00	0.86	0.14
5	120	2.06·10^{-6}	3.75	11.49 ± 1.00	0.00	0.87	0.13
5	720	1.13·10^{-7}	5.04	12.46 ± 1.08	–[‡]	–	–
5	1440	1.13·10^{-7}	5.04	12.46 ± 1.08	0.00	0.18	0.82
5	2160	1.13·10^{-7}	5.04	12.46 ± 1.08	0.00	0.21	0.79
5	3600	1.13·10^{-7}	5.04	12.46 ± 1.08	0.00	0.14	0.86
		[Fe^{2+}_{eql}] ≈ 3·10^{-6} M at pH 7					
7	168	1.83·10^{-5}	2.16	2.62 ± 0.23	0.95	0.05	0.00
7	1440	1.13·10^{-7}	5.04	12.46 ± 1.08	0.00	0.21	0.79

[*] k represents the magnitude of the slope obtained from the linear regression of the Se(IV) fraction between the initial point and the time when the lowest Se(IV) fraction is first attained in Fig. 7.
[‡] Kinetic samples in Fig. 2 were not measured by XAFS due to limited beamtime and thus not displayed in Figs. 3–6.
[a] Error of [Se]$_{eql}$ ± 4.8 %.
[b] Error shown in Fig. 2.
[c] Error of fraction ± 0.05.

et al. (Yalçıntaş et al., 2016). Using only the spectra of the Se reacted clays in each series (i.e., without references), we identified either two or three spectral components (i.e., chemical species) depending on the clay types. About 20 potential reference spectra out of a database, including e.g. red Se(0), grey Se(0), ferroselite, FeSe, and polyselenide, were then added step by step to reconstruct the experimental spectra and assess their statistical contribution.

With one exception (spectrum 4 of reduced STx-1), all spectra in each clay series were well reconstructed with sorbed selenite plus either one or two of the elemental Se references (Figs. 3–6). While reduced STx-1 and low-reduced NAu-2 required only the addition of red Se(0), reduced SWy-2 and high-reduced NAu-2 required also the addition of grey Se(0) to obtain a good reconstruction of chi and FTM spectra. Note that the presence of grey Se(0) is also revealed in XANES spectra by a more articulated post-edge dip (at the position of the blue hatched line marking the Se(IV) peak). In none of the samples we observed the formation of FeSe or $FeSe_2$.

While the XANES of spectrum 4 of reduced STx-1 was accurately reconstructed, differences primarily arose in the chi function. In the k range of 2 to 6 Å^{-1}, the oscillation pattern matched that of Se(IV) but with lower amplitude, whereas in the 6–12 Å^{-1} range, the oscillation pattern closely resembled that of red Se(0). No other Se species components could be identified to match this spectrum, and the intensity of Se-O and Se-Se_1 peaks in the Fourier transformation magnitude (FTM) aligned well with the trend of Se reduction. Hence, the imperfect reconstruction of spectrum 4 may result from oscillation interference between two Se components.

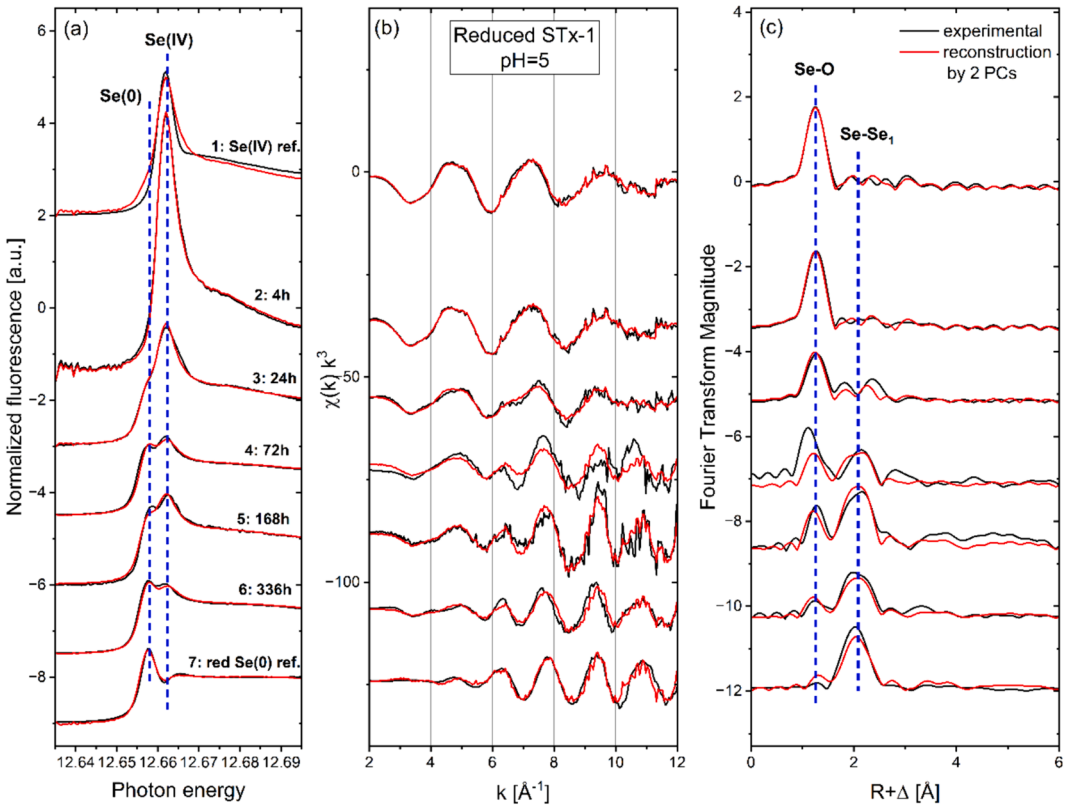

Fig. 3. Se K-edge XAFS of selenite sorption and reduction kinetics on reduced STx-1 at S/L of 2 g/L, $[Se]_{init} = 3{\cdot}10^{-5}$ M, 2 mM acetate buffer, 0.1 M NaCl, and pH 5. Samples were chosen from the kinetics experiments (Fig. 2) The black solid lines are the experimental data. The red solid lines represent the reconstruction of the spectra with two components: Se(IV) and red Se(0), and the blue dash line shows the position of each peak. (a) Normalized Se absorption edge (XANES), (b) k^3-weighted EXAFS chi function, (c) k^3-weighted EXAFS Fourier transform magnitude.

3.4. Se reduction

The fraction of each component consisting of the EXAFS spectra was determined in all clay samples by iterative target test (ITT) (Rossberg et al., 2003) (Fig. 7). In reduced STx-1, selenite gradually underwent reduction to red Se(0), without complete reduction or observation of grey Se(0) within the examined time range. Reduced SWy-2 displayed a faster reduction of selenite compared to reduced STx-1 and complete reduction was achieved. After 3600 h, red Se(0) was almost completely replaced by grey Se(0). In contrast to these clays with lower Fe content, selenite reduction was (almost) instantaneous by both reduced NAu-2 samples, with the degree of Fe reduction influencing the final product. With low-reduced NAu-2, only red Se(0) formed, while with high-reduced NAu-2, red Se(0) was formed initially, but was then gradually replaced by grey Se(0). Based on the observed trends of reduction behavior, the reduction kinetics of selenite appear to be correlated to the Fe(II) content of the clays.

To further substantiate this observation, we plotted $[Se(IV)]_t$ against time and fitted a linear regression between the initial Se(IV) fraction and the time when the lowest Se(IV) fraction was first obtained. The slope of this regression line can be considered as an apparent zero-order kinetics constant k of selenite reduction (Table 3). As already suggested by visual inspection, reduction kinetics exhibit a linear positive relationship (R^2 = 0.97) with Fe(II) content in clay (Fig. 8). In addition to the selenite reduction rate, the time needed to form grey Se(0) is probably also influenced by Fe(II) content. Comparing the formation of grey Se(0) in Fig. 7b and 7d, high-reduced NAu-2 requires less time to form grey Se(0) than reduced SWy-2. The correlation between Fe(II) content and grey Se (0) formation rate needs to be further studied with more Fe(II)-bearing clay samples and extended reaction time.

The decrease of red Se(0) and the increase of grey Se(0) at the same time indicated transformation of red Se(0) to grey Se(0). Red Se(0) is a metastable form of elemental selenium, existing as either an amorphous structure consisting of loosely stacked 8-rings, or a crystalline, monoclinic configuration of 8-rings, while grey Se(0) is the stable state of trigonal elemental selenium, characterized by spiral chains of Se atoms (Scheinost et al., 2008). Formation of red Se(0) resulting from selenite reduction has been observed in various minerals, including montmorillonite (Scheinost et al., 2008), siderite (Scheinost et al., 2008), green rust (Myneni et al., 1997), pyrite (Breynaert et al., 2008), and Fe(II)-sorbed calcite (Chakraborty et al., 2010). Grey Se(0) has been reported on magnetite (Poulain et al., 2022) and natural pyrite (Curti et al., 2013). Reaction conditions varied largely across these selenite reduction reactions, which makes it difficult to derive the factors determining formation of red or grey elemental Se. One notable observation is, however, that the presence of both elemental Se(0) species was noted on pyrite around pH 8 with red Se(0) forming after 3 weeks (Breynaert et al., 2008) and grey Se(0) forming after 8 months (Curti et al., 2013). This is in agreement with our study, where formation of red Se(0) required less time than that for grey Se(0) on the same clay mineral. And interesting question is the possible mechanism leading to the observed transformation of solid-state red Se to solid-state grey Se. Conventionally, the transformation of red Se(0) to grey Se(0) is achieved via high-pressure heating (Minaev et al., 2005; Wiberg and Wiberg, 2001). However, in this experiment, conducted under ambient conditions, one of the key distinguishing factors is the Fe(II) content within the clays. Note that owing to its additional Se-Se bond and structural arrangement, crystalline grey Se(0) exhibits metallic conductivity (Greenwood and Earnshaw, 2012). It is hence plausible that a continuous electron transfer facilitates the sharing of electrons among adjacent atoms and thus prompts the formation of Se-Se bonds (Persch et al., 2021). High-reduced NAu-2, possessing a higher concentration of Fe

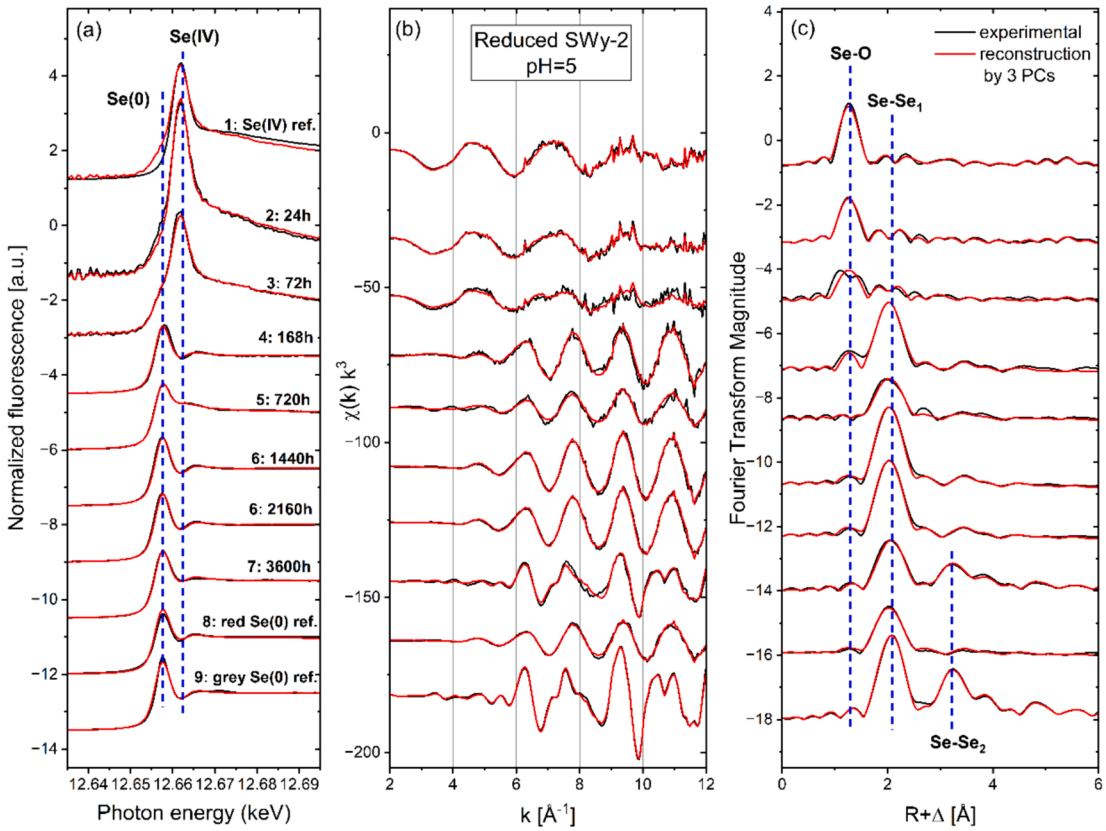

Fig. 4. Se K-edge XAFS of selenite sorption and reduction kinetics on reduced SWy-2 at S/L of 2 g/L, $[Se]_{init} = 3{\cdot}10^{-5}$ M, 2 mM acetate buffer, 0.1 M NaCl, and pH 5. Samples were chosen from the kinetics experiments (Fig. 2) The black solid lines are the experiment data. The red solid lines represent the reconstruction of the spectra with three components: Se(IV), red Se(0), and grey Se(0), and the blue dash line shows the position of each peak. (a) Normalized Se absorption edge (XANES), (b) k^3-weighted EXAFS chi function, (c) k^3-weighted EXAFS Fourier transform magnitude.

atoms within its structure, likely promotes faster electron transfer when compared to reduced SWy-2 with lower structural Fe content. As for the three types of dioctahedral smectite clays in this study, Fe is predominantly located in the octahedral sheets (Van Olphen et al., 1979) (as opposed to tetrahedral sheets which are occupied mostly by Si or Al). In addition to Fe(II) content, the Fe distribution in the octahedral sheet may be also an important factor to the final reduction products. According to Vantelon et al, SWy-2 displays an ordered distribution of Fe in the octahedral sheet, while STx-1 displays extensive Fe clustering (Vantelon et al., 2003). Hence, despite STx-1 having a low Fe(II) content of 0.6 wt%, electron transfer remains feasible for selenite reduction possibly due to this Fe clustering. Nonetheless, the precise impact of electron transfer kinetics and Fe(II) quantity on the structural transformation between red and grey Se(0) species remains elusive. To address this, future studies could employ clays with the same structure but varying reduction levels over extended reaction times.

In addition to elemental Se(0) being the prevalent reduction product, several investigations have documented formation of FeSe precipitates during selenite sorption onto mackinawite, magnetite, green rust, pyrite, zerovalent iron, and iron hydroxides (Börsig et al., 2018; Breynaert et al., 2008; Diener et al., 2012; López de Arroyabe Loyo et al., 2008; Olegario et al., 2010; Scheinost and Charlet, 2008; Scheinost et al., 2008). All these investigations highlighted the correlation between iron selenide formation and selenite reduction kinetics and presence of Fe^{2+} ($2.8–77{\cdot}10^{-3}$ M in equilibrium). Fast selenite reduction kinetics in the presence of Fe^{2+} fosters the formation of FeSe; observation of FeSe within 30 min up to several hours was reported in the literature. Moreover, reduction kinetics are directly associated with the size and surface condition of the iron minerals. Nanominerals (2–50 nm) possess a high specific surface area, which enhances reduction kinetics. In addition, the iron sulfide mackinawite FeS contains not only Fe(II) but also S(−II) in the system, acting as electron donor to reduce Se(IV). However, in our study, no FeSe or $FeSe_2$ was observed, and a slower reduction kinetics was observed, spanning from days to months. In contrast to the literature reported equilibrium Fe^{2+} concentration of 10^{-3} M, the results of this study reveal that the concentration of Fe^{2+} in the supernatant of the sorption experiment at both pH 5 and 7 (Table 3) is several orders of magnitude lower. Additionally, the initial selenite concentration of $10^{-2}–10^{-4}$ M is higher than the $3{\cdot}10^{-5}$ M used in this study. Moreover, compared to the nanomaterials (2–50 nm) mentioned in these references, the clay minerals investigated here possess larger particle sizes (< 500 nm), potentially leading to slower reduction kinetics. Notably, the surface conditions of reduced clays displayed minimal alteration in terms of the cation exchange capacity (Table 2) and the availability of surface complexation edge sites (Fig. 1) when compared to native clays. Consequently, we observed exclusively elemental Se(0) as the selenite reduction product.

3.5. *Structure of the initial selenite sorption complex*

Since previous research has demonstrated that formation of a covalent bond between adsorbed selenite and the clay edges is a prerequisite for its subsequent reduction (Charlet et al., 2007), the structure of this intermediate sorption complex in our samples is of substantial interest. Spectra 1 and 2 (Fig. 5), corresponding to adsorbed selenite, exhibit an additional peak at 2.8 Å (uncorrected for phase shift), which could point to backscattering from a clay surface atom and hence towards formation of an inner-sphere sorption complex. Fig. 9a compares the spectra of adsorbed selenite on native STx-1, SWy-2, and NAu-2. Only NAu-2 displays a clear peak at 2.8 Å (uncorrected for phase shift), while the peak is

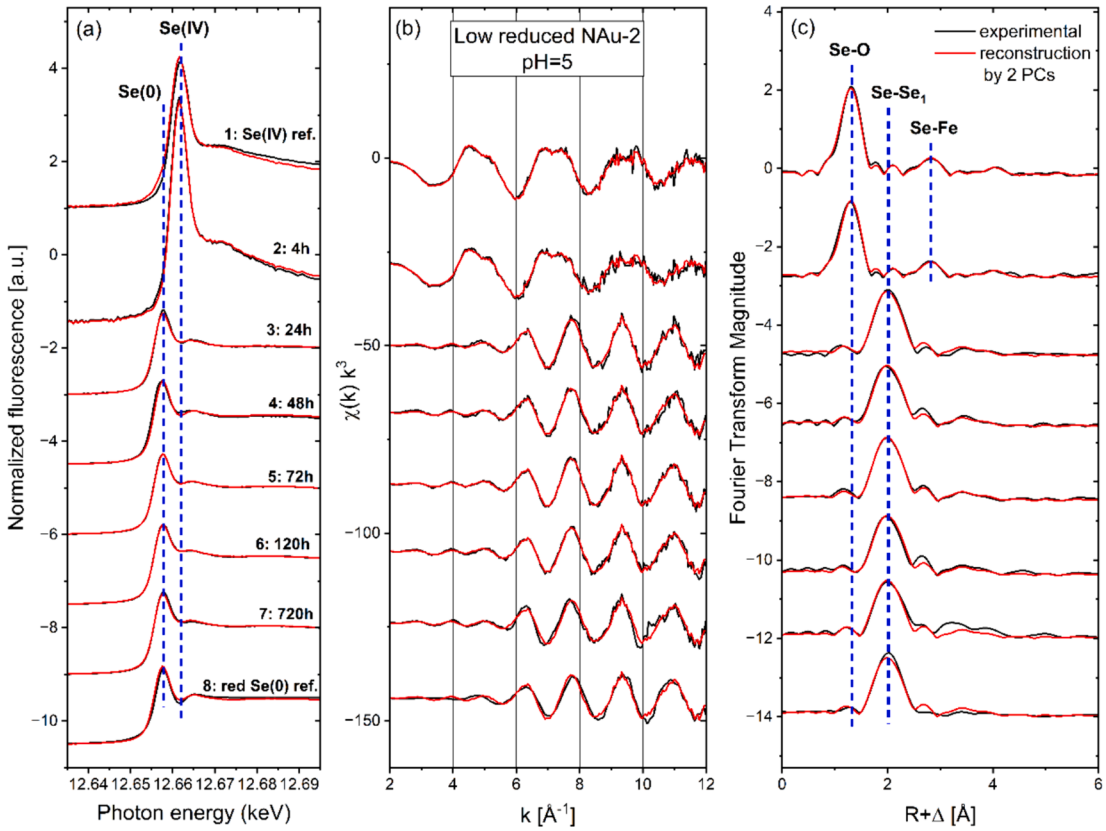

Fig. 5. Se K-edge XAFS of selenite sorption and reduction kinetics on low-reduced NAu-2 at S/L of 2 g/L, $[Se]_{init} = 3{\cdot}10^{-5}$ M, 2 mM acetate buffer, 0.1 M NaCl, and pH 5. Samples were chosen from the kinetics experiment (Fig. 2) The black solid lines are experiment data. The red solid lines represent the reconstruction of the spectra with two components: Se(IV) and red Se(0), and the blue dash line shows the position of each peak. (a) Normalized Se absorption edge (XANES), (b) k^3-weighted EXAFS chi function, (c) k^3-weighted EXAFS Fourier transform magnitude.

less evident in STx-1 and SWy-2. The Fourier backtransform of this peak shown in Fig. 9b has an envelope maximum at about 8 $Å^{-1}$ in line with backscattering from Fe, while the maximum for Al would be about 2 $Å^{-1}$ lower. This was confirmed by a successful shell fit, resulting in 2.7 O atoms at 1.69 Å in line with the typical local coordination of selenite (Scheinost et al., 2008), and 1.4 Fe atoms at 3.24 Å indicative for the inner-sphere sorption complex (Table 4). Previous studies (Börsig et al., 2021; Jordan et al., 2014; Manceau and Charlet, 1994) have reported two Se-Fe distances at 2.9 Å and 3.4 Å on magnetite, maghemite, and hydrous ferric oxide, corresponding to bidentate mononuclear edge-sharing (ES) and bidentate binuclear corner-sharing (CS) inner-sphere surface complexes, respectively. In our study, the Se-Fe peak does not show splitting, but rather exhibits a mean bond length of 3.24 Å, roughly in between the distances of 2.9 and 3.4 Å expected for ES and CS structures, thus probably pointing to a mixture of both ES and CS inner-sphere complexes at Fe-occupied octahedra of clay edges. As for selenite sorption on montmorillonite, Peak et al. demonstrated bidentate binuclear inner-sphere complexation with Se-Al distances at 3.16 Å (Peak et al., 2006), while others only fitted with Se-O shell (Charlet et al., 2007; Scheinost et al., 2008). The Se-Al distances fitted for the two clays with lower Fe content (Table 4) are at 3.11 and 3.18 Å, which aligns with the fitting results of Peak et al. (Peak et al., 2006), and their CN of 1.2 and 0.8 point to the prevalence of ES inner-sphere sorption complexes with Al-occupied octahedra. The spectroscopy results corroborate the modelling of the Se sorption data with a surface complexation reaction by Missana et al. (2009). In addition, Zhang et al. have proposed a two-step selenite adsorption mechanism on goethite involving the initial formation of outer-sphere surface complexes followed by a ligand-exchange process to form inner-sphere surface complexes (Zhang and Sparks, 1990).

3.6. Redox potential of clays

In this section, we show the results of selected Se reduction kinetics performed at pH 7, with the aim to separate the influence of redox potential from that of pH, as the redox potential for selenite reduction decreases as pH increases. The redox potential plays a crucial role in determining whether a redox reaction can occur (Masscheleyn et al., 1990). The E_h–pH diagram of Se (Fig. 10) illustrates the Se species distribution as a function of E_h and pH. The kinetics of selenite sorption at pH 7 are depicted in Fig. 11. After 168 h, selenite shows no reduction on reduced STx-1, partial reduction on reduced SWy-2, and no reduction on high-reduced NAu-2. The unexpected non-reduction of selenite observed in high-reduced NAu-2 after 7 days is intriguing, as it reduces selenite and forms gray Se(0) at the fastest rate at pH 5 and is anticipated to show a similar redox behavior at pH 7. As the reaction time extends to 1440 h, selenite is reduced to red Se(0) on reduced STx-1, transformed to grey Se(0) on reduced SWy-2, and also converted to grey Se(0) on high-reduced NAu-2. This indicates that selenite can still undergo reduction at pH 7, albeit at a much slower rate.

One notable difference is the amount of selenite sorption, which is generally lower at pH 7 compared to pH 5 (Table 3). However, despite displaying a lower sorption amount at pH 5 (0.70 mmol/kg, 4 h) compared to pH 7 (2.62 mmol/kg, 168 h), high-reduced NAu-2 still exhibits complete reduction at pH 5 and zero reduction at pH 7. Therefore, the selenite sorption amount does not appear to be the primary factor driving the unexpected selenite reduction behavior of high-reduced NAu-2. The variation in the selenite reduction behavior at different pH can be attributed to the disparity in the reducing potential required for selenite to be reduced to Se(0) (Fig. 11). Specifically, at pH 7, a lower reducing potential is necessary for the reduction of selenite to

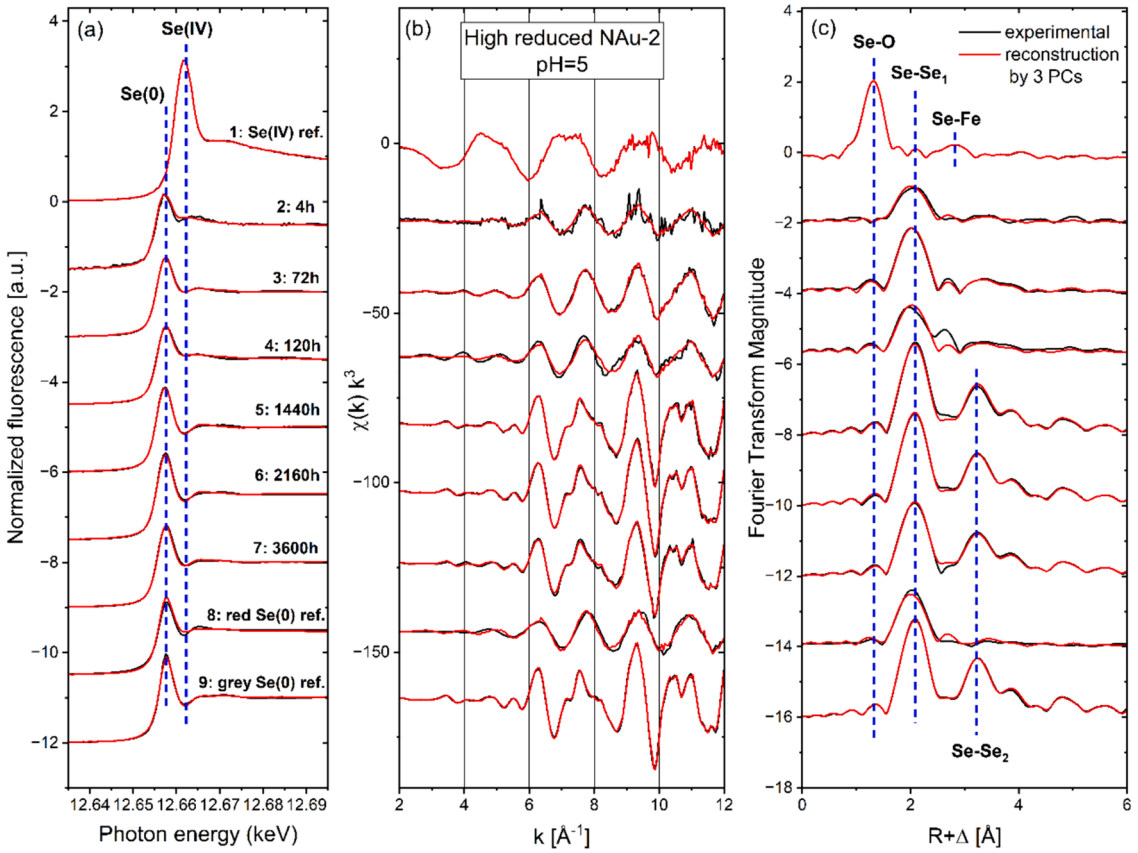

Fig. 6. Se K-edge XAFS of selenite sorption and reduction kinetics on high-reduced NAu-2 at S/L of 2 g/L, $[Se]_{init} = 3{\cdot}10^{-5}$ M, 2 mM acetate buffer, 0.1 M NaCl, and pH 5. Samples were chosen from the kinetics experiment (Fig. 2) The black solid lines are the experiment data. The red solid lines represent the reconstruction of the spectra with three components: Se(IV), red Se(0), and grey Se(0), and the blue dash line shows the position of each peak. (a) Normalized Se absorption edge (XANES), (b) k^3-weighted EXAFS chi function, (c) k^3-weighted EXAFS Fourier transform magnitude.

Se(0) as compared to pH 5.

The redox potential of the reduced clays was determined by MEO/MER measurements (Fig. 12). By applying the degree of reduction for each clay, the redox potential associated with the clay can be inferred from the redox profile (Gorski et al., 2013). Both reduced STx-1 (Fe(II)/Fe_{tot}: 0.89) and reduced SWy-2 (Fe(II)/Fe_{tot}: 1.0) exhibit a redox potential of approximately −0.4 V, while both low-reduced (Fe(II)/Fe_{tot}: 0.19) and high-reduced NAu-2 (Fe(II)/Fe_{tot}: 0.58) have a significantly higher redox potential of about 0.05 V (Fig. 12). The redox potentials of our reduced clays are similar to those reported by Gorski et al. (2013). The redox potential of reduced NAu-2 is higher than that of reduced STx-1 and reduced SWy-2. Hence, we suspect that selenite adsorbed on high-reduced NAu-2 was not reduced after 168 h due to the small potential difference between clay and selenite, whereas reduced SWy-2 exhibited easier initiation of selenite reduction owing to the larger potential difference. However, as the contact time increased, with sufficient electron transfer occurring from Fe(II) in high-reduced NAu-2 to the adsorbed selenite, selenite was eventually reduced. In the case of reduced STx-1, despite the redox potential being sufficient to initiate selenite reduction, selenite remained unreduced after 168 h. This could be attributed to the relatively low Fe(II) content in reduced STx-1, which hinders efficient electron transfer within a short period for selenite reduction. Nevertheless, with sufficient contact time, selenite can still undergo reduction. At pH 5, the potential required to reduce selenite is higher compared to that at pH 7. Therefore, it is likely that the redox potentials of the four reduced clays are sufficient to initiate selenite reduction, indicating that it is not a limiting factor for this process. Note that the E_h–pH diagram illustrates the Se species in equilibrium, while the E_h measured by MEO/MER represents the initial redox potential of the clay and can be used to assess the progress of a redox reaction. Consequently, the overall reduction process is influenced not only by the redox potential of the clays, which initiates the redox reaction, but also by the experimental condition like pH. Gorski et al. observed that all smectites exhibited unique Fe(II)/Fe_{tot} − E_h relationship, which correlated with structural properties of clays (Gorski et al., 2013). However, it is not yet clear how these properties affect the redox potential of clays, but they may manifest in the redox reaction under different experimental conditions and need further study.

The redox potential of the reduced STx-1 and SWy-2 suggests the possibility of selenite reduction to HSe^- (Table S1). However, XAFS does not detect any Se species associated with the mineral phase other than Se (0). Moreover, R_d increases consistently over time, while we would expect a temporary drop of R_d, if a significant amount of HSe^- would form as an intermediate species (which is assumed to sorb weakly). Of course, these observations do not allow us to exclude the formation of aqueous Se(−II) species, especially if they are not associated with the clay phase.

While formation of elemental Se(0) was observed even under conditions where the solution phase was thermodynamically predicted to be undersaturated with respect to this solid phase, the lower detection limit of XAFS prevented us from going significantly below an initial Se concentration of $3{\cdot}10^{-5}$ M (low surface loading, see isotherm in SI). Therefore, we could not extent our study to conditions, where Se(0) eventually might not form a polymeric solid anymore.

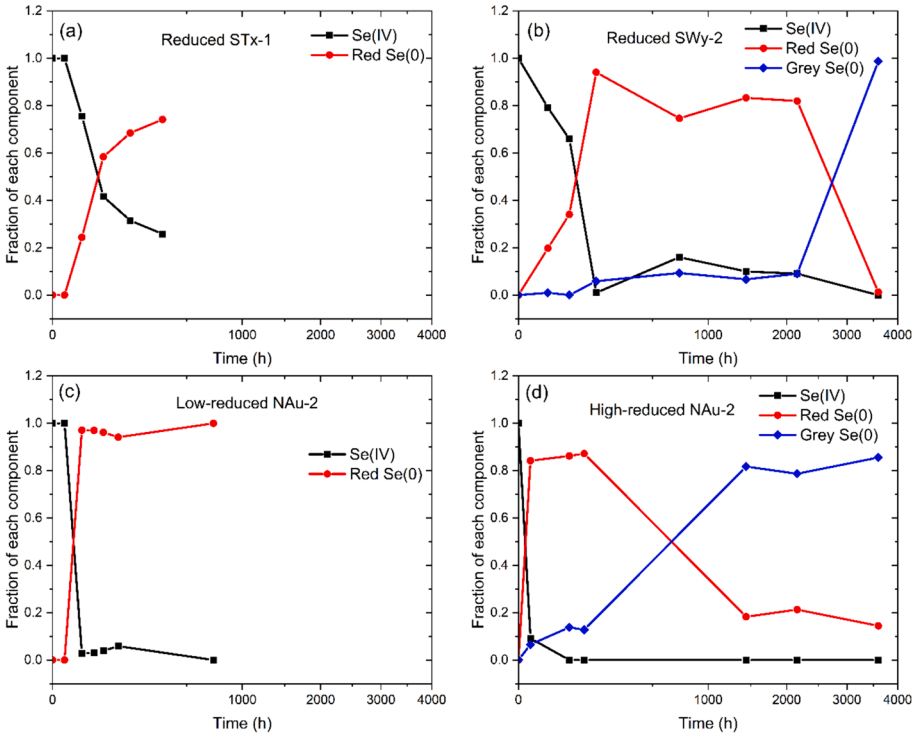

Fig. 7. Fraction of selenite Se(IV) (black square lines), red Se(0) (red dot lines), and grey Se(0) (blue diamond lines) for each kinetics experiment with reduced clays (reduced STx-1, reduced SWy-2, low-reduced NAu-2, and high-reduced NAu-2) at different reaction time. X-axis is in logarithm scale. Fractions are derived from the chi spectra in Figs. 3–6 by ITT.

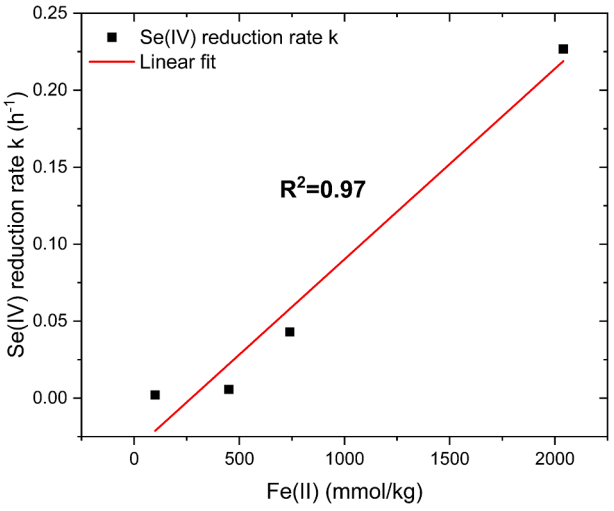

Fig. 8. Correlation between Fe(II) content in the clay and Se(IV) reduction rate k (Table 3).

3.7. Implications

We investigated selenite immobilization by Fe-bearing smectite clays under a relatively large range of physicochemical parameters, including redox potential, pH, Fe(II) content, clay mineral, and thermodynamic solubility range, which allow to apply the results of our study to the geochemistry of selenium under different conditions, including natural environments and radioactive waste repositories.

Our study affirms the capability of Fe-bearing clay minerals to effectively impede selenite mobility by adsorption and reduction processes, ultimately converting it into insoluble elemental Se(0). Furthermore, the transformation of elemental Se(0) from its initial amorphous red state to the thermodynamically more stable crystalline grey polymorph underscores the significant potential for immobilizing selenite, thus safeguarding surrounding ecosystems. Elemental Se(0) formed even under conditions where it was not thermodynamically predicted.

Overall, these findings on selenite immobilization are highly relevant in the context of environmental risk assessment associated with its bioavailability. It has implications for ecosystem protection and human health, highlighting the importance of understanding and implementing effective strategies for selenite immobilization.

4. Conclusion

We systematically investigated the kinetics of selenite adsorption and reduction across four reduced clay minerals, characterized by Fe(II) and Fe(III) contents and associated redox potentials, under different pH conditions. We observed adsorption and reductive precipitation in selenite sorption mechanism. Selenite reduction occurred on all the reduced clays, initially forming amorphous or nanoparticle red Se(0) which gradually transformed into thermodynamically more stable crystalline grey Se(0). The transformation of red Se(0) into grey Se(0) can be understood as the kinetically hindered conversion of an amorphous (or less crystalline) solid phase into the thermodynamically stable and more crystalline form of the solid. No FeSe or $FeSe_2$ was detected under an initial selenite concentration of $3{\cdot}10^{-5}$ M and equilibrium Fe^{2+} concentration of up to $6{\cdot}10^{-4}$ M at pH 5 within 3600 h. Selenite reduction rate is proportional to the structural Fe(II) content in the clay

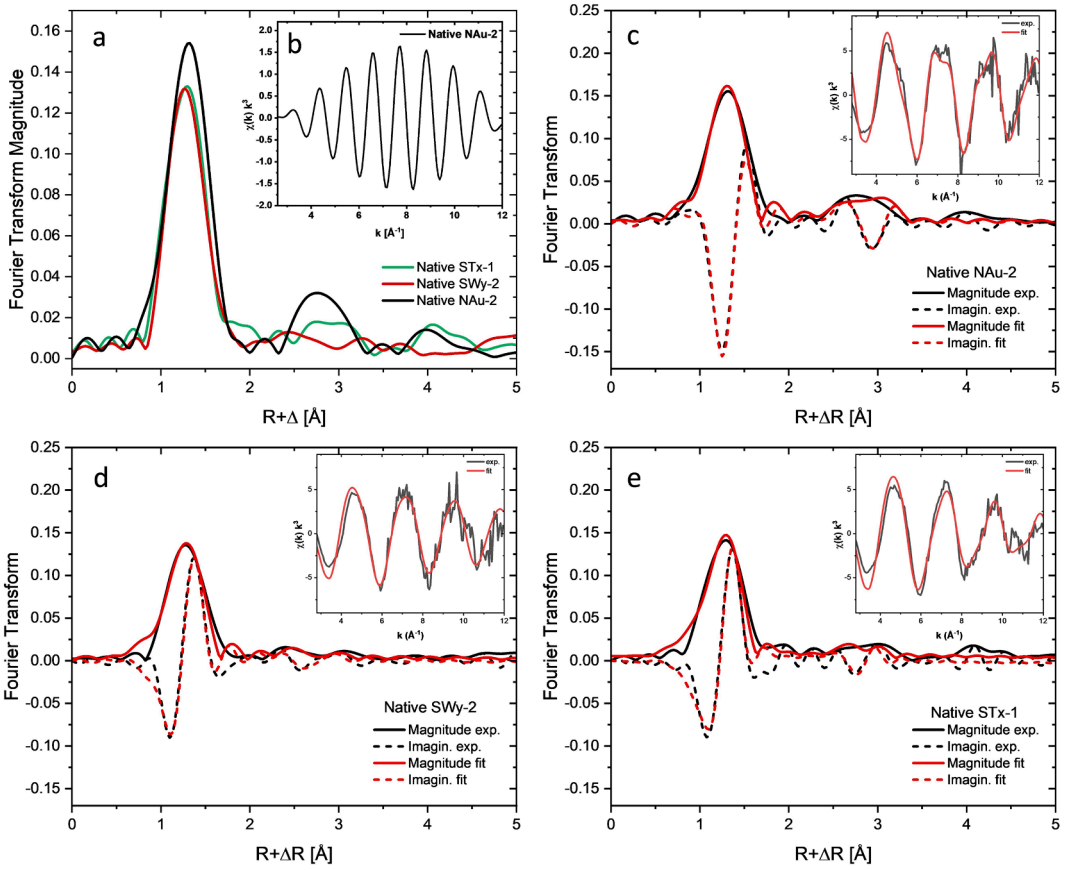

Fig. 9. (a) Comparison of Fourier transform magnitude of Se(IV) sorption on native STx-1, SWy-2, and NAu-2. (b) Fourier backtransform of the second peak (R: 2.3–3.3 Å) of native NAu-2. (c)–(e) Shell fitting of native NAu-2, SWy-2, and STx-1 in R space; the fitted spectra in k space are inserted.

Table 4
Se K-edge shell fitting results for selenite sorption complexes.

Sample	Shell	CN[a]	R [Å][b]	σ^2 [Å^2][c]	ΔE_0 [eV]	S_0^2	χ_{Res}
Native	Se-O	3.6	1.69	0.0054	13.7	0.9*	17.9
STx-1	Se-Al	0.8	3.18	0.0015			
Native	Se-O	2.6	1.69	0.0024	13.4	0.9*	15.5
SWy-2	Se-Al	1.2	3.11	0.0077			
Native	Se-O	2.7	1.69	0.0011	13.3	0.9*	17.2
NAu-2	Se-Fe	1.4	3.24	0.0046			

[a] Error of coordination number (CN) ± 25 %.
[b] Error of radial distance (R) ± 0.01 Å.
[c] Error of Debye-Waller factor (σ^2) ± 0.002 Å.
* S_0^2 fixed to 0.9.

minerals at pH 5. At pH 7, selenite reduction still took place, albeit at a slower rate compared to pH 5, attributed to a narrower potential difference between clays and selenite. Under current experiment conditions, the determining factor of selenite reduction is the structural Fe(II) content at pH 5, while it is the redox potential of clays at pH 7. Overall, the selenite reduction behavior is controlled by different factors, including the redox potential of the clays, electron transfer at the interface (e.g., inner-sphere surface complex), and experimental conditions (e.g. pH, [Se(IV)], time). The redox potential of the clay is related to the total Fe content, redox active Fe, Fe(II)/Fe(III) ratio, and Fe distribution within the structure. Future research should focus on one specific clay with varying reduction levels to investigate individual parameters more closely. Furthermore, employing a higher selenite solution concentration can help ascertain whether [Se(IV)] plays a decisive role in the formation of FeSe or $FeSe_2$.

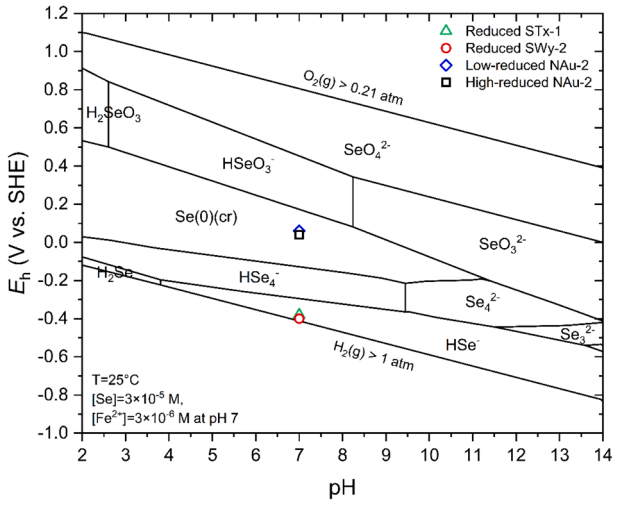

Fig. 10. E_h–pH diagram of Se-O-H system at 25 °C, [Se] = $3{\cdot}10^{-5}$ M, and [Fe^{2+}] = $3{\cdot}10^{-6}$ M ([Fe^{2+}] is Fe^{2+}_{eql} determined in sorption experiments at pH 7), plotted by PhreePlot using the PSI Chemical Thermodynamic Database 2020 (Hummel and Thoenen, 2023), which does not distinguish between red and grey elemental Se(0). The redox potentials of reduced clays measured by MEO & MER at pH 7 are also shown (green triangle: reduced STx-1, red circle: reduced SWy-2, blue diamond: low-reduced NAu-2, black square: high-reduced NAu-2).

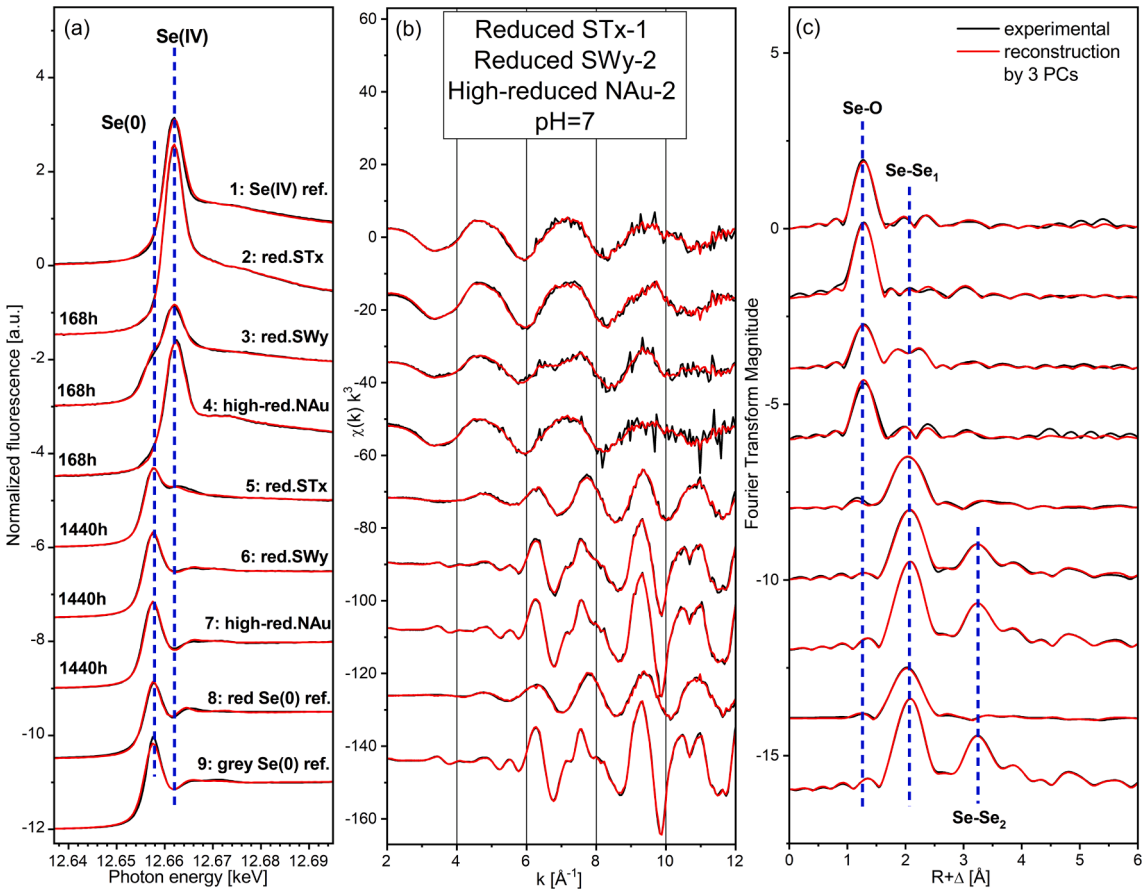

Fig. 11. Se K-edge EXAFS of selenite sorption and reduction kinetics on reduced STx-1, reduced SWy-2, and high-reduced NAu-2 at S/L of 2 g/L, $[Se]_{init} = 3{\cdot}10^{-5}$ M, 2 mM MOPS buffer, 0.1 M NaCl, and pH 7. The kinetics experiment results of the samples were listed in Table 3. The experiment data is in black solid line, the red solid line represents the reconstruction of the spectra with three components: Se(IV), red Se(0), and grey Se(0), and the blue dash line shows the position of each peak. (a) Normalized Se absorption edge (XANES), (b) k^3-weighted EXAFS chi function, (c) k^3-weighted EXAFS Fourier transform magnitude.

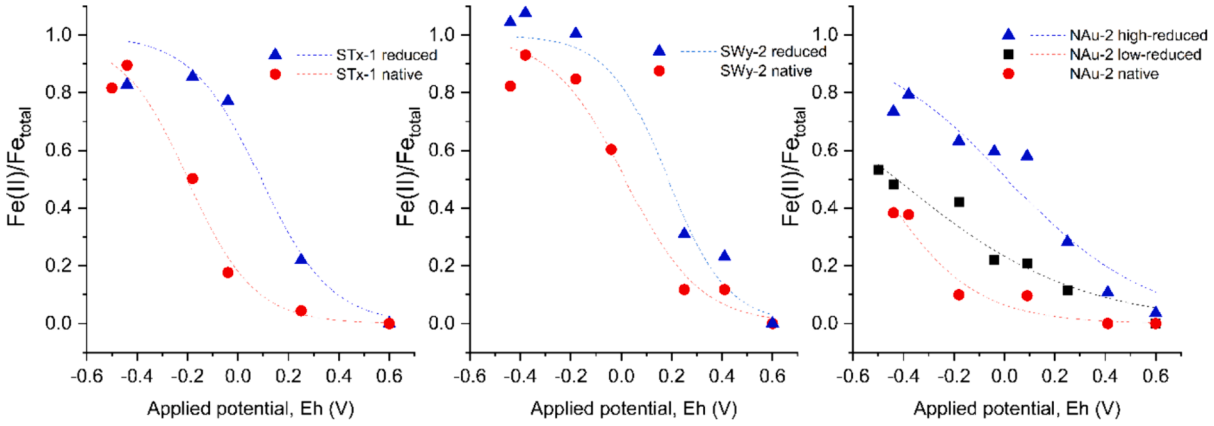

Fig. 12. Redox profiles of native and reduced STx-1, SWy-2, and NAu-2 measured by MEO & MER at pH 7.

CRediT authorship contribution statement

Yanting Qian: Investigation, Writing – original draft, Writing – review & editing. **Andreas C. Scheinost:** Data curation, Supervision, Writing – review & editing, Formal analysis, Methodology, Writing – original draft. **Sylvain Grangeon:** Investigation. **Alwina Hoving:** Methodology. **Sergey V. Churakov:** Supervision. **Maria Marques Fernandes:** Conceptualization, Investigation, Project administration, Supervision, Writing – original draft, Writing – review & editing.

Declaration of competing interest

The authors declare that they have no known competing financial interests or personal relationships that could have appeared to influence the work reported in this paper.

Data availability

Data are available through Mendeley Data at https://doi.org/10.17632/6m72h529xb.1.

Acknowledgement

This work was supported by European Union's Horizon 2020 research and innovation program under grant agreement No. 847593. Beamtime at the Rossendorf Beamline at ESRF was provided by ESRF and HZDR. We thank Astrid Schaible and Andreas Laube for laboratory technical support, Dr. Bin Ma for insightful discussions on the results, and Jörg Exner for assisting with EXAFS measurements.

Appendix A. Supplementary material

The supplementary material for this study includes three figures (Fig. S1, S2, S3) and one table (Table S1). Fig. S1 displays the preliminary results of selenite sorption edge and sorption isotherm. Fig. S2 shows the selenite sorption and reduction kinetics on reduced clays in ppm. Fig. S3 compares the Se K-edge XANES spectra of different Se(IV) references. Table S1 shows the predicted Se mineral saturation indices and activities of dominant aqueous species under the experimental conditions. Supplementary material to this article can be found online at https://doi.org/10.1016/j.gca.2024.05.012.

References

Baeyens, B., Bradbury, M.H., 2004. Cation exchange capacity measurements on illite using the sodium and cesium isotope dilution technique: effects of the index cation, electrolyte concentration and competition: modeling. Clays Clay Miner. 52, 421–431.

Baeyens, B., Marques Fernandes, M., 2018. 5 - Adsorption of heavy metals including radionuclides. In: Schoonheydt, R., Johnston, C.T., Bergaya, F. (Eds.), Developments in Clay Science. Elsevier, pp. 125–172.

Bingham, P.A., Connelly, A.J., Cassingham, N.J., Hyatt, N.C., 2011. Oxidation state and local environment of selenium in alkali borosilicate glasses for radioactive waste immobilisation. J. Non Cryst. Solids 357, 2726–2734.

Börsig, N., Scheinost, A.C., Shaw, S., Schild, D., Neumann, T., 2017. Uptake mechanisms of selenium oxyanions during the ferrihydrite-hematite recrystallization. Geochim. Cosmochim. Acta 206, 236–253.

Börsig, N., Scheinost, A.C., Shaw, S., Schild, D., Neumann, T., 2018. Retention and multiphase transformation of selenium oxyanions during the formation of magnetite via iron(ii) hydroxide and green rust. Dalton Trans. 47, 11002–11015.

Börsig, N., Scheinost, A.C., Schild, D., Neumann, T., 2021. Mechanisms of selenium removal by partially oxidized magnetite nanoparticles for wastewater remediation. Appl. Geochem. 132, 105062.

Bradbury, M.H., Baeyens, B., 2002. Sorption of Eu on Na- and Ca-montmorillonites: experimental investigations and modelling with cation exchange and surface complexation. Geochim. Cosmochim. Acta 66, 2325–2334.

Breynaert, E., Bruggeman, C., Maes, A., 2008. XANES−EXAFS analysis of Se solid-phase reaction products formed upon contacting Se(IV) with FeS_2 and FeS. Environ. Sci. Technol. 42, 3595–3601.

Chakraborty, S., Bardelli, F., Charlet, L., 2010. Reactivities of Fe(II) on calcite: selenium reduction. Environ. Sci. Technol. 44, 1288–1294.

Charlet, L., Scheinost, A.C., Tournassat, C., Greneche, J.-M., GÉhin, A., Fernandez-Martinez, A., Coudert, S., Tisserand, D., Brendle, J., 2007. Electron transfer at the mineral/water interface: selenium reduction by ferrous iron sorbed on clay. Geochim. Cosmochim. Acta 71, 5731–5749.

Charlet, L., Kang, M., Bardelli, F., Kirsch, R., Géhin, A., Grenèche, J.-M., Chen, F., 2012. Nanocomposite pyrite–greigite reactivity toward Se(IV)/Se(VI). Environ. Sci. Technol. 46, 4869–4876.

Curti, E., Aimoz, L., Kitamura, A., 2013. Selenium uptake onto natural pyrite. J. Radioanal. Nucl. Chem. 295, 1655–1665.

Curti, E., Puranen, A., Grolimund, D., Jädernas, D., Sheptyakov, D., Mesbah, A., 2015. Characterization of selenium in UO_2 spent nuclear fuel by micro X-ray absorption spectroscopy and its thermodynamic stability. Environ. Sci. Processes Impacts 17, 1760–1768.

Diener, A., Neumann, T., Kramar, U., Schild, D., 2012. Structure of selenium incorporated in pyrite and mackinawite as determined by XAFS analyses. J. Contam. Hydrol. 133, 30–39.

Fernández-Martínez, A., Charlet, L., 2009. Selenium environmental cycling and bioavailability: a structural chemist point of view. Rev. Environ. Sci. Bio/technol. 8, 81–110.

Fordyce, F.M., 2013. Selenium deficiency and toxicity in the environment. In: Selinus, O. (Ed.), Essentials of Medical Geology, Revised Edition. Springer, Netherlands, Dordrecht, pp. 375–416.

Frasca, B., Savoye, S., Wittebroodt, C., Leupin, O.X., Michelot, J.L., 2014. Comparative study of Se oxyanions retention on three argillaceous rocks: Upper Toarcian (Tournemire, France), Black Shales (Tournemire, France) and Opalinus Clay (Mont Terri, Switzerland). J. Environ. Radioact. 127, 133–140.

Frechou, C., Aguerre, S., Degros, J.-P., Kerlau, G., Grangeon, T., 2007. Improvement of a radiochemical separation for selenium 79: applications to effluents and nuclear wastes. Talanta 72, 1166–1171.

Gorski, C.A., Klupfel, L., Voegelin, A., Sander, M., Hofstetter, T.B., 2012. Redox properties of structural Fe in clay minerals. 2. Electrochemical and spectroscopic characterization of electron transfer irreversibility in ferruginous smectite, SWa-1. Environ. Sci. Technol. 46, 9369–9377.

Gorski, C.A., Klupfel, L.E., Voegelin, A., Sander, M., Hofstetter, T.B., 2013. Redox properties of structural Fe in clay minerals: 3. Relationships between smectite redox and structural properties. Environ. Sci. Technol. 47, 13477–13485.

Greenwood, N.N., Earnshaw, A., 2012. Chemistry of the Elements. Elsevier.

Hammouh, F., Zein, S., Amr, R., Ghazzawi, H., Muharib, D., Al, S.D., Subih, H., 2021. Assessment of dietary selenium intake of Jordanian adults in Madaba: a cross sectional study. Nutr. Food Sci. 51, 494–506.

Hoving, A.L., Sander, M., Bruggeman, C., Behrends, T., 2017. Redox properties of clay-rich sediments as assessed by mediated electrochemical analysis: separating pyrite, siderite and structural Fe in clay minerals. Chem. Geol. 457, 149–161.

Huang, J., Jones, A., Waite, T.D., Chen, Y., Huang, X., Rosso, K.M., Kappler, A., Mansor, M., Tratnyek, P.G., Zhang, H., 2021. Fe(II) Redox chemistry in the environment. Chem. Rev. 121, 8161–8233.

Hummel, W., Thoenen, T., 2023. The PSI chemical thermodynamic database 2020, Nagra Technical Report NTB 21-03. Nagra, Wettingen, Switzerland.

Jaisi, D.P., Liu, C., Dong, H., Blake, R.E., Fein, J.B., 2008. Fe2+ sorption onto nontronite (NAu-2). Geochim. Cosmochim. Acta 72, 5361–5371.

Jordan, N., Lomenech, C., Marmier, N., Giffaut, E., Ehrhardt, J.-J., 2009. Sorption of selenium(IV) onto magnetite in the presence of silicic acid. J. Colloid Interface Sci. 329, 17–23.

Jordan, N., Ritter, A., Foerstendorf, H., Scheinost, A.C., Weiß, S., Heim, K., Grenzer, J., Mücklich, A., Reuther, H., 2013. Adsorption mechanism of selenium(VI) onto maghemite. Geochim. Cosmochim. Acta 103, 63–75.

Jordan, N., Ritter, A., Scheinost, A.C., Weiss, S., Schild, D., Hübner, R., 2014. Selenium (IV) uptake by maghemite (γ-Fe_2O_3). Environ. Sci. Technol. 48, 1665–1674.

Li, S., Xiao, T., Zheng, B., 2012. Medical geology of arsenic, selenium and thallium in China. Sci. Total Environ. 421–422, 31–40.

López de Arroyabe Loyo, R., Loyo, R., Nikitenko, S.I., Scheinost, A.C., Simonoff, M., 2008. Immobilization of selenite on Fe_3O_4 and Fe/Fe_3C ultrasmall particles. Environ. Sci. Technol. 42, 2451–2456.

Ma, B., Charlet, L., Fernandez-Martinez, A., Kang, M., Madé, B., 2019. A review of the retention mechanisms of redox-sensitive radionuclides in multi-barrier systems. Appl. Geochem. 100, 414–431.

MacFarquhar, J.K., Broussard, D.L., Melstrom, P., Hutchinson, R., Wolkin, A., Martin, C., Burk, R.F., Dunn, J.R., Green, A.L., Hammond, R., Schaffner, W., Jones, T.F., 2010. Acute selenium toxicity associated with a dietary supplement. Arch. Intern. Med. 170, 256–261.

Manceau, A., Charlet, L., 1994. The mechanism of selenate adsorption on goethite and hydrous ferric oxide. J. Colloid Interface Sci. 168, 87–93.

Marques Fernandes, M., Baeyens, B., 2020. Competitive adsorption on illite and montmorillonite: experimental and modelling investigations, Nagra Technical Report NTB 19-05. Nagra, Wettingen, Switzerland.

Masscheleyn, P.H., Delaune, R.D., Patrick Jr., W.H., 1990. Transformations of selenium as affected by sediment oxidation-reduction potential and pH. Environ. Sci. Technol. 24, 91–96.

Minaev, V.S., Timoshenkov, S.P., Kalugin, V.V., 2005. Structural and phase transformations in condensed selenium. J. Optoelectron. Adv. Mater. 7, 1717–1741.

Missana, T., Alonso, U., García-Gutiérrez, M., 2009. Experimental study and modelling of selenite sorption onto illite and smectite clays. J. Colloid Interface Sci. 334, 132–138.

Moreno-Reyes, R., Egrise, D., Nève, J., Pasteels, J.-L., Schoutens, A., 2001. Selenium deficiency-induced growth retardation is associated with an impaired bone metabolism and osteopenia. J. Bone Miner. Res. 16, 1556–1563.

Myneni, S.C.B., Tokunaga, T.K., Brown, G.E., 1997. Abiotic selenium redox transformations in the presence of Fe(II, III) oxides. Science 278, 1106–1109.

Olegario, J.T., Yee, N., Miller, M., Sczepaniak, J., Manning, B., 2010. Reduction of Se(VI) to Se(-II) by zerovalent iron nanoparticle suspensions. J. Nanopart. Res. 12, 2057–2068.

Onoguchi, A., Granata, G., Haraguchi, D., Hayashi, H., Tokoro, C., 2019. Kinetics and mechanism of selenate and selenite removal in solution by green rust-sulfate. R. Soc. Open Sci. 6, 182147.

Oremland, R.S., Stolz, J., 2000. Dissimilatory reduction of selenate and arsenate in nature. In: Environmental Microbe-Metal Interactions. pp. 199–224.

Peak, D., Saha, U.K., Huang, P.M., 2006. Selenite adsorption mechanisms on pure and coated montmorillonite: an EXAFS and XANES spectroscopic study. Soil Sci. Soc. Am. J. 70, 192–203.

Pearce, C.I., Coker, V.S., Charnock, J.M., Pattrick, R.A.D., Mosselmans, J.F.W., Law, N., Beveridge, T.J., Lloyd, J.R., 2008. Microbial manufacture of chalcogenide-based nanoparticles via the reduction of selenite using Veillonella atypica: an in situ EXAFS study. Nanotechnology 19, 155603.

Peigneur, P., 1976. Stability and adsorption affinity of some transition metal-amine complexes in aluminosilicates. Univ Leuven, Belgium (Ph.D Thesis).

Perrin, Dempsey, 1974. Buffers for pH and Metal Ion Control. Chapman and Hall, London.

Persch, C., Müller, M.J., Yadav, A., Pries, J., Honné, N., Kerres, P., Wei, S., Tanaka, H., Fantini, P., Varesi, E., Pellizzer, F., Wuttig, M., 2021. The potential of chemical bonding to design crystallization and vitrification kinetics. Nat. Commun. 12, 4978.

Poulain, A., Fernandez-Martinez, A., Greneche, J.-M., Prieur, D., Scheinost, A.C., Menguy, N., Bureau, S., Magnin, V., Findling, N., Drnec, J., Martens, I., Mirolo, M., Charlet, L., 2022. Selenium nanowire formation by reacting selenate with magnetite. Environ. Sci. Technol. 56, 14817–14827.

Qian, Y., Scheinost, A.C., Grangeon, S., Greneche, J.-M., Hoving, A., Bourhis, E., Maubec, N., Churakov, S.V., Fernandes, M.M., 2023. Oxidation state and structure of

Fe in nontronite: from oxidizing to reducing conditions. ACS Earth Space Chem. 7, 1868–1881.
Rayman, M.P., 2012. Selenium and human health. Lancet 379, 1256–1268.
Ressler, T., 1998. WinXAS: a program for X-ray absorption spectroscopy data analysis under MS-Windows. J. Synchrotron Radiat. 5, 118–122.
Rodriguez, D.M., Mayordomo, N., Scheinost, A.C., Schild, D., Brendler, V., Müller, K., Stumpf, T., 2020. New insights into 99Tc(VII) removal by pyrite: a spectroscopic approach. Environ. Sci. Technol. 54, 2678–2687.
Rojo, H., Scheinost, A.C., Lothenbach, B., Laube, A., Wieland, E., Tits, J., 2018. Retention of selenium by calcium aluminate hydrate (AFm) phases under strongly-reducing radioactive waste repository conditions. Dalton Trans. 47, 4209–4218.
Rossberg, A., Reich, T., Bernhard, G., 2003. Complexation of uranium (VI) with protocatechuic acid—application of iterative transformation factor analysis to EXAFS spectroscopy. Anal. Bioanal. Chem. 376, 631–638.
Scheinost, A.C., Charlet, L., 2008. Selenite reduction by mackinawite, magnetite and siderite: XAS characterization of nanosized redox products. Environ. Sci. Technol. 42, 1984–1989.
Scheinost, A.C., Kirsch, R., Banerjee, D., Fernandez-Martinez, A., Zaenker, H., Funke, H., Charlet, L., 2008. X-ray absorption and photoelectron spectroscopy investigation of selenite reduction by FeII-bearing minerals. J. Contam. Hydrol. 102, 228–245.
Scheinost, A.C., Claussner, J., Exner, J., Feig, M., Findeisen, S., Hennig, C., Kvashnina, K. O., Naudet, D., Prieur, D., Rossberg, A., Schmidt, M., Qiu, C., Colomp, P., Cohen, C., Dettona, E., Dyadkin, V., Stumpf, T., 2021. ROBL-II at ESRF: a synchrotron toolbox for actinide research. J. Synchrotron Radiat. 28, 333–349.
Soltermann, D., Marques, F.M., Baeyens, B., Miehe-Brendle, J., Dahn, R., 2014. Competitive Fe(II)-Zn(II) uptake on a synthetic montmorillonite. Environ. Sci. Technol. 48, 190–198.
Stucki, J., Golden, D., Roth, C., 1984. Preparation and handling of dithionite-reduced smectite suspensions. Clays Clay Miner. 32, 191–197.
Tan, L.C., Nancharaiah, Y.V., van Hullebusch, E.D., Lens, P.N., 2016. Selenium: environmental significance, pollution, and biological treatment technologies. Biotechnol. Adv. 34, 886–907.
Titov, A.F., Kaznina, N.M., Karapetyan, T.A., Dorshakova, N.V., Tarasova, V.N., 2022. Role of selenium in plants, animals, and humans. Biol. Bull. Rev. 12, 189–200.
Tournassat, C., Grangeon, S., Leroy, P., Giffaut, E., 2013. Modeling specific pH dependent sorption of divalent metals on montmorillonite surfaces. a review of pitfalls, recent achievements and current challenges. Am. J. Sci. 313, 395–451.
Van Olphen, H., Fripiat, J.J., Organisation for Economic Co-operation and Development, Clay Minerals Society, 1979. Data Handbook for Clay Materials and Other Non-metallic Minerals: Providing Those Involved in Clay Research and Industrial Application with Sets of Authoritative Data Describing the Physical and Chemical Properties and Mineralogical Composition of the Available Reference Materials. Pergamon Press.
Vantelon, D., Montarges-Pelletier, E., Michot, L.J., Pelletier, M., Thomas, F., Briois, V., 2003. Iron distribution in the octahedral sheet of dioctahedral smectites. An Fe K-edge X-ray absorption spectroscopy study. Phys. Chem. Miner. 30, 44–53.
Volfson, I.F., Farrakhov, E.G., Pronin, A.P., Beiseyev, O.B., Beiseyev, A.O., Bogdasarov, M.A., Oderova, A.V., Pechenkin, I.G., Khitrov, A.E., Pikhur, O.L., 2010. Medical geology in Russia and the NIS. In: Medical Geology: A Regional Synthesis. Springer, pp. 221–258.
Webb, S.M., 2005. SIXpack: a graphical user interface for XAS analysis using IFEFFIT. Phys. Scr. 2005, 1011.
Wiberg, E., Wiberg, N., 2001. Inorganic Chemistry. Academic Press.
Winkel, L.H.E., Johnson, C.A., Lenz, M., Grundl, T., Leupin, O.X., Amini, M., Charlet, L., 2012. Environmental selenium research: from microscopic processes to global understanding. Environ. Sci. Technol. 46, 571–579.
Yalçıntaş, E., Scheinost, A.C., Gaona, X., Altmaier, M., 2016. Systematic XAS study on the reduction and uptake of Tc by magnetite and mackinawite. Dalton Trans. 45, 17874–17885.
Zhang, P., Sparks, D.L., 1990. Kinetics of selenate and selenite adsorption/desorption at the goethite/water interface. Environ. Sci. Technol. 24, 1848–1856.